University of Regensburg Institute of Physics

Magnetotransport in altermagnetic CrSb

Master's thesis

by

Christoph Müller

January 15, 2025

Reviewer:	Prof. Dr. Jörg Wunderlich
Second Reviewer:	Prof. Dr. Christoph Strunk
Supervisors:	Dr. Dominik Kriegner, Prof. Dr. Jörg Wunderlich

Contents

Abstract

Compensated magnets with a spin-split nonrelativistic band structure have gained significant interest in spintronics research over recent years. These materials are referred to as altermagnets. In this work, the altermagnetic Chromium Antimonide (CrSb) is thoroughly investigated in both bulk form and as epitaxial thin films. Magnetometry measurements using a SQUID magnetometer confirm the vanishing net magnetization, while X-ray diffraction (XRD) analysis validates the hexagonal NiAs phase of CrSb, also ensuring high structural quality.

Detailed magnetotransport studies reveal distinct differences between the bulk and thin-film systems. The ordinary magnetoresistance (OMR) exhibits a substantial change, with bulk samples showing variations in the tens of percent range, whereas in thin films, the OMR drops significantly to sub-percent levels. Additionally, the Hall resistivity in the bulk samples shows a pronounced nonlinear slope, which is identified to arise from multi-carrier transport in connection with high-mobility carriers. In contrast, this nonlinear behavior is absent in the thin films, indicating distinct transport dynamics between the two material forms.

A carrier analysis further highlights the differences in Hall resistivity in greater detail, while underscoring that the dominant hole-like transport remains consistent in both bulk and thin-film systems. The analysis reveals that while both systems share this dominant transport mechanism, the carrier densities and mobilities vary significantly. The calculated mobilities in bulk are approximately 100 times higher than in thin films, whereas the carrier density in bulk is about 20 times lower than in thin films. Magnetotransport measurements were also conducted at the high-field facility Helmholtz-Zentrum Dresden-Rossendorf (HZDR) to investigate potential high-field effects, such as spin-flop or spin-flip transitions. However, these phenomena were not observed. Additionally, none of the conducted experiments provide evidence for the occurrence of the anomalous Hall effect (AHE). This study underlines the impact of dimensionality and sample preparation on the transport properties of CrSb and its potential role in the field of altermagnetism.

While samples for this thesis were provided by collaborators, the characterization work was performed by the author unless otherwise stated.

Motivation

For over 50 years, expanding the capacity and performance of data storage devices has been a significant challenge for both the scientific community and the tech industry. The pursuit of innovative concepts in this area is highly valued, particularly given the increasing demands of sectors such as artificial intelligence, telecommunications, and entertainment. Consequently, the analysis and development of new materials and mechanisms, such as semiconductors and transistors, are pivotal in driving the enhancement of modern technological capabilities. Although the well-known *Moore's Law* predicts a continuous increase in the functionality of digital electronics within a specified cost, power, and chip size, experts now anticipate this growth to stagnate around 2025 [1]. This stagnation is attributed, among other factors, to the fact that state-of-the-art transistors are approaching atomic scales, and the costs associated with their fabrication are rising significantly [1]. The exploration of alternative concepts and materials is therefore a pressing task in science and research.

When it comes to data storage units like hard disk drives (HDD), (ferro-)magnetic materials offer distinct advantages over alternatives such as semiconductors [2]. These advantages include their ability to store large amounts of data nonvolatilely, as well as their robustness and cost-effectiveness [2]. However, their relatively slow data transfer rates make them unsuitable for applications like random-access memory (RAM), a domain currently dominated by transistor technologies [3]. A promising solution that combines the benefits of magnetism with the fast read and write speeds of transistors lies in the field of *spintronics*. This field leverages the intrinsic property of electron *spin* (and its associated magnetic moment) in addition to the charge considered in conventional *electronics* [4]. The incorporation of spin is motivated, among other factors, by the expectation of achieving lower power consumption [4]. Additionally, advancements in spin-based phenomena such as spin torques and magnetoresistances have the potential to enable the development of high-performance computing systems, particularly through the implementation of magnetic RAM (MRAM) technology [5]. Although Louis Néel claimed in his Nobel Lecture 1970 that the discovery of antiferromagnets is interesting but useless [6], these materials aroused interest over the last decades in spintronics since they have typically much faster dynamics than ferromagnets [5]. The antiparallel alignment of neighboring sublattices in antiferromagnets, resulting in zero net magnetization, has led to the observation that antiferromagnetic materials interact less with nearby atoms compared to ferromagnetic materials [5]. This property may enable a higher data storage density [5]. Efficient and reliable manipulation of antiferromagnets is a fundamental concept underpinning all antiferromagnetic spintronics applications [7]. While ferromagnets are known since thousands of years and antiferromagnets conquered spintronics over the last decade, recently a third magnetic phase called *altermagnetism* got introduced, showing some highly interesting properties and effects which can't be explained using only the traditionally two basic magnetic phases [8].

This thesis explores the magnetotransport phenomena of altermagnetic Chromium Antimonide (CrSb). Chapter 1 introduces the origins of magnetic order and distinguishes between various magnetic phases. Further, the crystallographic and magnetic properties of CrSb are examined in Chapter 2 to ensure the altermagnetic phase in bulk and thin-film samples. The third chapter provides a brief overview of magnetotransport concepts. Chapter 4 focuses on the magnetotransport properties of both bulk and thin-film CrSb, while their differences and similarities are analyzed and discussed in Chapter 5.

1 Introduction

Magnetic phases generally emerge from the interactions between atoms and/or electrons within solids. These interactions govern the alignment of magnetic moments, leading to the formation of various magnetic orders. To be precise, the magnetic moment m of atoms depends on their electronic structure while the magnetic order of the multitude of atoms in solids is the product of various types of interactions between themselves. The following sections will explain those interactions and demonstrate that magnetic order is closely linked to symmetry.

1.1 Origins of Magnetic Order

Ferromagnetic materials (FM) are crucial in spintronics, as they provide a source of spin polarised carriers [9]. In most textbooks, the first approach to explaining ferromagnetism is the introduction of the *Weiss model*, which assumes that there is an effective molecular field that leads to the parallel alignment of the magnetic moments of the atoms, resulting in a spontaneous magnetization M that remains even without an external applied field [10]. Further, the alignment itself creates the molecular field responsible for the initial alignment, resulting in a causality dilemma [10]. A more comprehensive framework, which incorporates the quantum properties of electrons and emphasizes the critical role of the *exchange interaction*, is more suitable for accurately describing such systems. In particular, the spin orientation of electrons in atoms affects the symmetry of the spatial wavefunction, $\psi(\vec{r})$, at position $\vec{r}$, as the total electron wavefunction, Ψ, must be antisymmetric [10]. In the case of a two-electron model, with a symmetric orbital ψ_s and an antisymmetric orbital ψ_a, the antibonding triplet state is described as:

$$\Psi_T = \frac{1}{\sqrt{2}}[\psi_s(\vec{r_1})\psi_a(\vec{r_2}) - \psi_s(\vec{r_2})\psi_a(\vec{r_1})]\chi_T \tag{1}$$

where χ_T represents the symmetric spin function ($\mathbf{S} = 1$) [10]. This state leads to a greater distance between the electrons, minimizing the Coulomb repulsion and resulting in a lower potential energy state:

$$E_T = \int \Psi_T^* \hat{H} \Psi_T d\vec{r_1}\vec{r_2} \tag{2}$$

with the Hamiltonian $\hat{H}$ [10]. However, due to the Pauli exclusion principle, one electron must occupy a higher state, increasing the kinetic energy [10]. The alternative state, the singlet state, is given by:

$$\Psi_S = \frac{1}{\sqrt{2}}[\psi_s(\vec{r_1})\psi_a(\vec{r_2}) + \psi_s(\vec{r_2})\psi_a(\vec{r_1})]\chi_S \tag{3}$$

where χ_S represents the antisymmetric spin function ($\mathbf{S} = 0$) [10]. This state is bonding and involves antiparallel spin configurations, but the electrons remain on the same orbital [10]. The energy of the singlet state is:

$$E_S = \int \Psi_S^* \hat{H} \Psi_S d\vec{r_1}\vec{r_2}[10]. \tag{4}$$

Thus, while the triplet state minimizes Coulomb repulsion, the singlet state results in bonding due to parallel spins [10]. This implies that only if the reduction of potential energy compensates the increase of kinetic energy the spin **S** is maximized and therefore a parallel alignment of the spins occurs [10]. Mathematically this leads to the definition of the *exchange integral*

$$J = \frac{E_S - E_T}{2} \tag{5}$$

and the effective Hamiltonian

$$\hat{H} = -2J\mathbf{S_1} \cdot \mathbf{S_2}[10]. \tag{6}$$

If $E_T > E_S$ or $J < 0$, the singlet state $\mathbf{S} = 0$ is favoured and the spins align antiparallel, while $J > 0$ implies that the triplet state $\mathbf{S} = 1$ with parallel aligned spins is preferred [10]. In case of a many-body system, the Hamiltonian from equation (6) evolves to the *Heisenberg Hamiltonian*

$$\hat{H} = -\sum_{i,j} J_{ij}\mathbf{S_i} \cdot \mathbf{S_j} \tag{7}$$

where the calculation of the exchange integrals J_{ij} gets quite complicated [10]. To determine whether a system can save energy by becoming ferromagnetic, one can verify if the *Stoner criterion* is satisfied:

$$U \cdot DOS(E_F) \geq 1[11]. \tag{8}$$

In this case U is the Coulomb energy and $DOS(E_F)$ represents the *density of states* at the Fermi-level. Further, the central result of this equation is that if the density of states at the Fermi-level and the Coulomb energy are large enough, the spin-up and spin-down bands will be split spontaneously by an energy ΔE due to exchange interaction [10]. This causes a net magnetization $M \neq 0$ in the absence of an external magnetic field. The direction of this spontaneous magnetization (easy axis) depends among others on the shape of the sample and, more importantly, on the crystal structure, also known as *magnetocrystalline anisotropy* [10].

As shown in Figure 1.1 the exchange interaction induces an energy shift between up- and down-spin electrons resulting in a significant difference in filling at the Fermi energy E_F. Crucial for this spin-splitting are, especially but not exclusively, the d-bands or more precisely the electrons which belong to the 3d orbitals [9]. They are affected the most by the crystal field derived from neighboring atoms which depends on the symmetry of the local environment [9]. As equation (8) demonstrates, the overlap of the wave-functions is of great importance to create magnetic order. In case of ions with partially filled 3d orbitals, the crystal field interaction predominates the spin-orbit interaction [9]. This contradicts Hund's rules, and therefore the third rule, which suggests that the total orbital angular momentum should be maximized, is incorrect[1] [9]. The 4f orbitals, however, are more close to the nucleus which has the consequences that the crystal field interaction is negligible and Hund's

[1]This effect is also called *orbital quenching*. Looking at various 3d ions and calculating $p = \frac{\mu_{eff}}{\mu_B}$ one can find that $p_S = 2\sqrt{\mathbf{S}(\mathbf{S}+1)}$ fits better with the experimental results than $p_J = g_J\sqrt{\mathbf{J}(\mathbf{J}+1)}$. This means that the systems choose a ground state where $\mathbf{L} = 0$ and therefore $\mathbf{J} = \mathbf{S}$ and $g_J = 2$ [10].

rules apply [9]. A key consequence of the spin-split density of states in spintronics is the resulting polarization of charge carriers [9]. Materials exhibiting high spin polarization are therefore highly valuable in applications that rely on spin transport [12]. The method of identifying ferromagnetic ordering using the Stoner criterion, which relies on analyzing the electronic band structure, is commonly referred to as *band magnetism*.

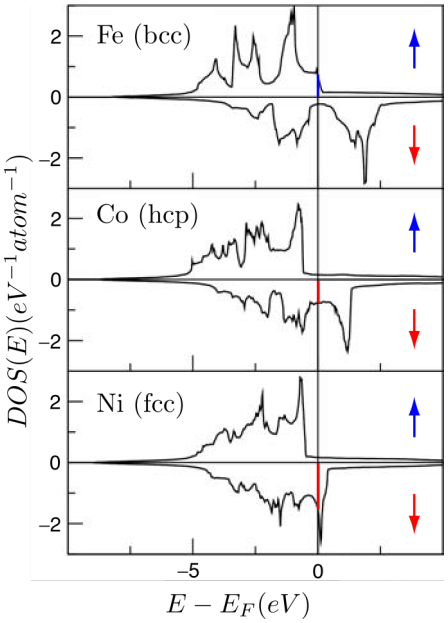

Figure 1.1: Density of states for various materials in the ferromagnetic phase, distinguishing between spin-up and spin-down bands. This figure is based on Ref. [9].

However, when the exchange integral J is negative, the magnetic moments will align antiparallel to their nearest neighbor, resulting in a zero net magnetization $M = 0$ [9]. More precisely, this results in two equal but oppositely oriented sublattices. Important to mention is that there are more types of compensated orders than the previously described *collinear* one. In triangular arrangements, for example, moments can be oriented such that they are not antiparallel to avoid frustration, yet the system remains compensated. This phenomenon is known as *noncollinear* ordering. A even more intricate configuration of magnetic moments involves their arrangement in a *coplanar* ordering, where the moments cancel each other out within a plane. However, this work focuses exclusively on collinear systems, as this is sufficient for the case of CrSb, where the alignment is collinear, as will be explained in subsequent sections.

Temperature is a key parameter for both uncompensated and compensated magnetic phases, as all magnetic order can be disrupted above a critical temperature [9]. For ferromagnetism, this constant is known as the Curie temperature T_C, while for compensated systems, it is referred to as the Néel temperature T_N. The critical temperature depends on many factors, most of which can be attributed to exchange interaction [9]. When the temperature exceeds the specific T_C or T_N, a system typically transitions to a paramagnetic state [9]. In this state, magnetic ordering is absent unless an external magnetic field is applied [9]. In case of ferromagnets the magnetization M grows with decreasing temperature until it reaches the saturation or maximum magnetization M_S at $T = 0$ K [9]. The same holds for the two sublattices of compensated systems as shown in Figure 1.2 [9].

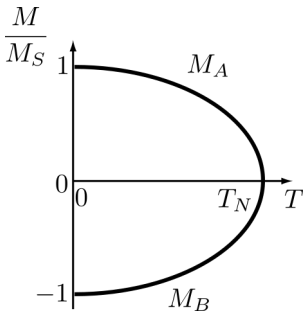

Figure 1.2: Magnetization of the two sublattices M_A and M_B of an compensated magnet depending on temperature. This figure is adapted from Ref. [9].

1.2 Effects of External Magnetic Fields

To describe how the three-dimensional magnetization $\vec{M}$ of a material changes in response to an external magnetic field $\vec{B}$, the *magnetic susceptibility* χ_{ij} is defined by the relation:

$$\chi_{ij} := \frac{\partial \vec{M}_i}{\partial \vec{B}_j} \tag{9}$$

where i and j denote the directions of the magnetization and applied field, respectively [13]. The magnetization vector, $\vec{M}$, tends to align with the direction of the applied external magnetic field [9]. The previously described molecular field theory provides a reliable framework for determining the (paramagnetic) susceptibility of ferromagnets above T_C, as it aligns well with experimental observations [9]. The susceptibility is given by:

$$\chi = \frac{C}{T - T_C} \tag{10}$$

where C is the Curie constant depending on the material [9]. At $T = T_C$, the susceptibility diverges, as shown in Figure 1.3. For compensated magnets above T_N, the susceptibility follows a similar behavior:

$$\chi = \frac{C}{T + T_N} [9]. \tag{11}$$

Let us now consider the temperature range below T_N in collinear ordered compensated magnetic systems. The magnetic easy axis is influenced by magnetocrystalline anisotropy, and the change in magnetization depends on the orientation of the external field relative to this axis [9]. This means there are two different temperature-dependent scalars for $\vec{B}$ parallel and perpendicular to the magnetic axis, namely $\chi_{\parallel}$ and $\chi_{\perp}$ [9]. For **small applied fields**, one can calculate these susceptibilities by expanding the Brillouin functions. It is found that $\chi_{\parallel}$ decreases with decreasing temperature, reaching zero at $T = 0$ K while $\chi_{\perp}$ remains constant as Figure 1.3 shows [9].

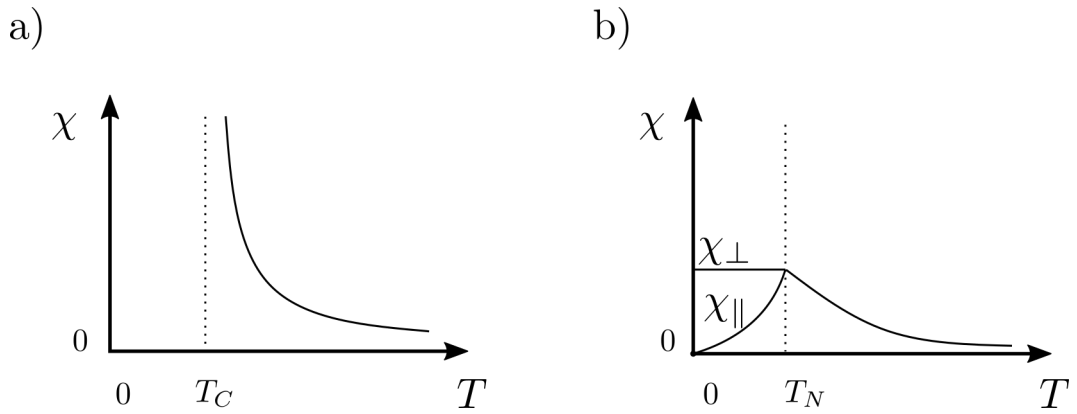

Figure 1.3: Temperature dependence of the magnetic susceptibility for a) a ferromagnet and b) a compensated magnet. This figure is adapted from Ref. [9].

In the case of a perpendicular to the magnetic axis applied field, the magnetization direction of both sublattices starts to cant slightly toward the same direction as $\vec{B}$, independent of temperature [10]. For the parallel to the magnetic axis applied field, the field has no effect, and the resulting net magnetization remains zero at 0 K [10]. For $0 < T < T_N$, thermal fluctuations lead to the enhancement of the magnetization of one of the sublattices until $\chi_{\parallel} = \chi_{\perp}$ at $T = T_N$ [10].

For **strong magnetic fields**, the perpendicular case remains unchanged. The sublattice magnetizations gradually rotate with increasing field strength until all moments align parallel to the field [9]. If a weak applied field is directed parallel to both sublattice magnetizations at $T = 0$, the moments do not change their direction [9]. At a certain critical field, the orientation of the sublattices changes abruptly, leading to one of two possible outcomes: *spin-flop* or *spin-flip* transitions [14, 10]. In a spin-flop transition, the sublattices reorient by 90 degrees at $B = B_{sf}$, causing the magnetic axis to become perpendicular to the applied field [9]. The moments concomitantly cant towards the field direction [9]. With increasing field strength, the moments align progressively more with the field until they become fully parallel, resulting in saturated magnetization at $B = B_s$ as shown in Figure 1.4 [9]. In contrast, a spin-flip transition involves an immediate 180-degree reversal of the antiparallel sublattice moments into alignment with the field, achieving full magnetization saturation instantaneously [9]. The reason for these phenomena lies in the reduction of the system's energy [9]. While the energy of the compensated state remains constant with the applied field, the energy of the spin-flop and spin-flip configurations decreases as the field strength increases [9]. One of these transitions occurs at the field where the energy of a specific configuration becomes lower than that of the compensated state [9]. Whether a spin-flop or spin-flip transition occurs depends on the magnetocrystalline anisotropy of the sublattices [9]. If the anisotropy is strong, the system directly saturates the magnetization via a spin-flip transition, whereas if the anisotropy is weak, a spin-flop transition will occur [9]. For $T \ll T_N$ the critical field B_{sf} can be calculated as

$$B_{sf} = 2\sqrt{B_a B_{ex}} \tag{12}$$

with the material-specific *anisotropy field* B_a and the *exchange field* B_{ex} resulting from the exchange integral J [9, 15]. The anisotropy field describes the field that is needed to saturate the magnetization of a uniaxial crystal in a hard direction [9].

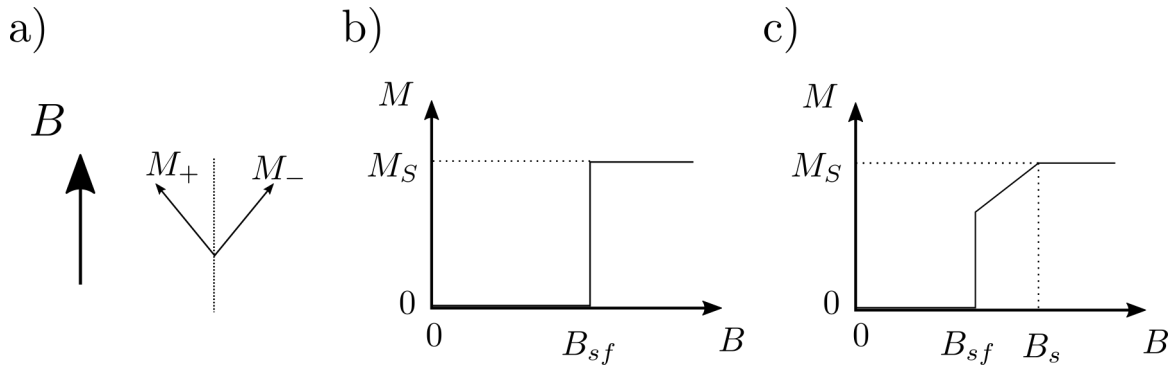

Figure 1.4: Effects of strong external magnetic fields. a) Configuration of the sublattices with magnetizations M_+ and M_- following a spin-flop transition. b) and c) Magnetization as a function of the field for spin-flip and spin-flop transitions, respectively. This figure is adapted from Ref. [9].

1.3 Magnetic Phases and the Emergence of Altermagnetism

The previously described magnetic ordering allowed only a distinction between $J > 0$, resulting in net magnetization, and $J < 0$, leading to vanishing net magnetization. Until the end of the last decade, it was generally assumed that $J < 0$ directly implied antiferromagnetic (AFM) ordering. However, recent studies have sparked interest in materials characterized by zero net magnetization and spin-split energy bands. This discovery led to the classification of a third distinct magnetic phase, referred as *altermagnetism*, which combines unique attributes from both ferromagnetism and antiferromagnetism [16]. Before the establishment of altermagnetism, the investigation of novel magnetic materials was predominantly guided by the formalism of magnetic-symmetry groups [16]. However, it is essential to recognize that these groups represent only a limited subset of the more extensive class of spin groups [17]. Moreover, they may overlook phases and phenomena that arise when considering the broader nonrelativistic spin-group formalism [16]. Those limitations can be overcome by employing the spin-group formalism, which accounts for pairs of transformations that will be introduced in this section [16]. The two advantages of this approach are that it yields a larger symmetry landscape due to the independent action of two distinct transformations and that it incorporates nonrelativistic electromagnetic crystal potentials [16]. Magnetic groups on the other hand are representing the relativistic limit. The dominance of the strong nonrelativistic crystal potentials justifies neglecting the comparatively weaker spin-orbit interaction effects in the following characterization using the spin-group formalism [16].

In general, spin groups can be expressed as a direct product $\boldsymbol{r_s} \times \boldsymbol{R_s}$, where $\boldsymbol{r_s}$ represents the spin-only group, and $\boldsymbol{R_s}$ denotes the nontrivial spin group containing elements of the form $[R_i||R_j]$ [16]. In this notation, the first transformation, R_i, acts exclusively within spin space, while the second transformation, R_j, operates within real space [16]. The spin-only group $\boldsymbol{r_s}$ provides a framework for identifying whether a system is magnetically ordered or disordered. In magnetically ordered systems, continuous spin rotations as symmetry operations are no longer allowed, marking a fundamental distinction from nonordered systems. Magnetically ordered systems can then be categorized into collinear systems or more complex arrangements such as noncollinear or coplanar systems. Collinear systems are characterized by a 180° spin rotation, referred to as a C_2 operation, which must exist because this spin rotation, when combined with a time-reversal operation, always remains a symmetry operation. In contrast, this symmetry does not hold in noncollinear systems. This work will focus exclusively on collinear magnetic ordering, as it is the relevant scenario for CrSb, which will be discussed in detail later. Importantly, $\boldsymbol{R_s}$ does not include any elements from the spin-only group $\boldsymbol{r_s}$ [17, 18]. By analyzing the nonrelativistic spin-only group $\boldsymbol{r_s}$ independently, it can be shown that the nonrelativistic electronic bands of all collinear magnets remain invariant under real-space inversion, even in the absence of inversion symmetry in the crystal structure [8]. Mathematically, this invariance implies that the energy $E(s, k)$ of bands, which depend on spin (s) and crystal momentum (k), satisfies the relation $E(s, k) = E(s, -k)$. Incorporating the nontrivial spin Laue groups $\boldsymbol{R_s}$, which include spin Laue groups in R_i and conventional Laue groups in R_j corresponding to real-space crystallographic transformations, enables the classification of three distinct magnetic phases [16]. The first type of nontrivial spin Laue group, or magnetic phase, is characterized by a nonrelativistic spin-split band structure, nonzero magnetization, and the breaking of time-reversal symmetry [16]. This phase corresponds to conventional collinear ferromagnetism and implies that the magnetic crystal structure consists of a single spin lattice [16]. The second phase exhibits spin-degenerate band energies $E(s, k)$ across all

k-vectors in the Brillouin zone [16]. Furthermore, the band structures are invariant under time-reversal symmetry, and the total magnetization is zero [16]. These characteristics classify this phase as conventional collinear antiferromagnetism, which led Néel to describe them as "useless" due to their spin-degenerate bands. In collinear antiferromagnetic spin arrangements, the spin configuration remains invariant under at least one of two distinct symmetry operations [16]. The first operation, $[C_2||t]$, involves a 180° spin rotation (C_2) combined with a real-space translation (t) that interchanges atomic positions [16]. The second operation, $\left[C_2||\bar{E}\right]$, similarly applies a 180° spin rotation but is accompanied by an inversion in real space ($\bar{E}$) [16]. Note that, in this case, the inversion center must lie between the two sublattices. Materials belonging to the third phase exhibit nonrelativistic spin-split band structures, broken time-reversal symmetry, and zero net magnetization [16]. This third altermagnetic phase also requires an even number of magnetic atoms within the unit cell [8]. Additionally, the nontrivial spin Laue group indicates the absence of an inversion center between magnetic sublattices [16]. Consequently, after a C_2 operation, the allowed real-space symmetry-preserving transformations between opposite spin sublattices cannot be achieved solely by translation or inversion but instead require rotations or combinations involving rotations [16]. In these systems, the band energies satisfy the condition $E(s,k) = E(-s,k')$ for $k \neq k'$ [16]. In this context, k and k' represent specific directions in reciprocal space that correspond to the real-space direction along which the symmetry-preserving transformation is executed. An example illustrating this third phase is the RuO_2 crystal, as shown in the following figure.

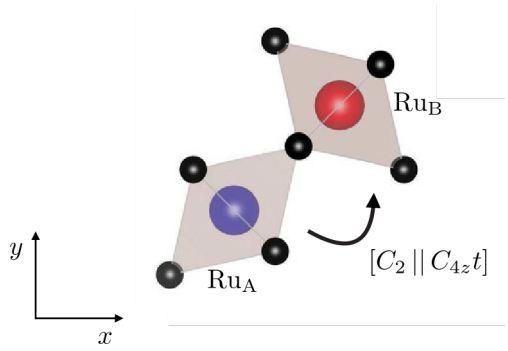

Figure 1.5: Schematic top view of the RuO_2 crystal, showing opposite spin directions on the Ru_A and Ru_B sublattices, highlighted in blue and red, respectively. The oxygen atoms are represented in black. The black arrow indicates a symmetry-preserving transformation comprising a 180° spin-space rotation (C_2) and a four-fold real-space rotation combined with a translation ($C_{4z}t$). This figure is taken from [16].

In several members of the rutile family, such as the metallic RuO_2 (Figure 1.5), the compensated antiparallel arrangement of magnetic moments was well known to Néel and his contemporaries. They introduced this configuration into the literature as a classical example of antiferromagnetism [19]. This concept was based on focusing exclusively on the lattice of magnetic atoms, disregarding the significant influence of nonmagnetic atoms on the symmetry in rutile crystals and similar compounds [16]. In detail, the altermagnetic spin-splitting arises from a local anisotropic electric crystal field generated by the crystal in the nonmagnetic phase [16]. Again, the key advantage of employing nonrelativistic spin groups combined with the nontrivial spin group $\boldsymbol{R_s}$ lies in their ability to provide a systematic symmetry description of magnetism, which emerges from strong nonrelativistic

electromagnetic crystal potentials [8]. Within this framework, the electric crystal potential is referred to as the internal potential in the nonmagnetic phase of the crystal, as described, for instance, by the local density approximation in density-functional theory (DFT) [8]. The oversight of the nonmagnetic potentials may partly explain why the unconventional alternating spin-splitting in the nonrelativistic band structures, remained unnoticed for almost a century [16]. This phenomenon is distinct from the conventional ferromagnetic splitting that arises from exchange interaction or spin-orbit coupling[2] (SOC). A schematic distinction among the three phases is presented in Figure 1.6.

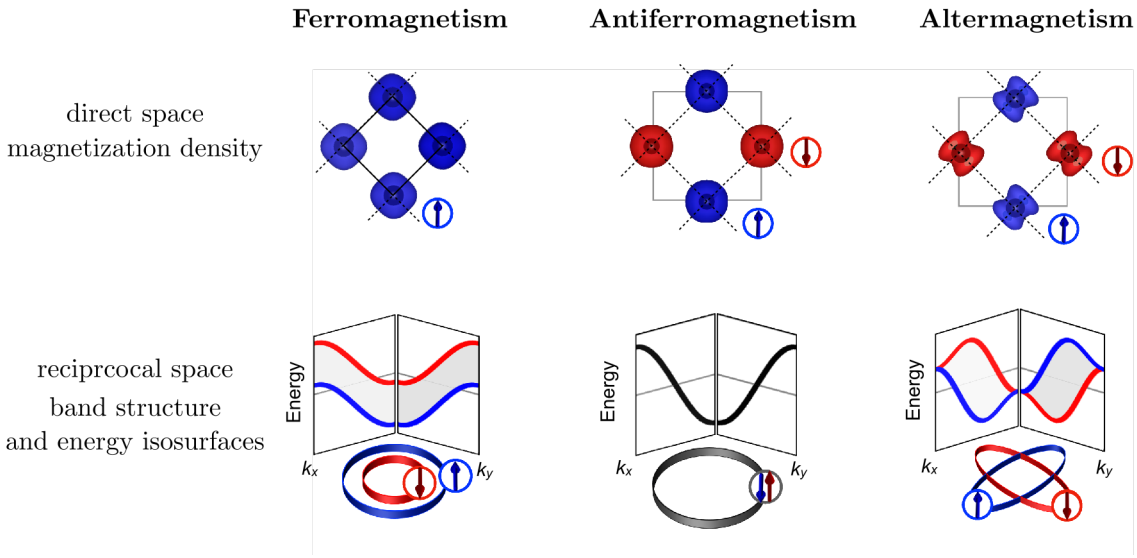

Figure 1.6: Magnetic phases exhibiting collinear magnetic order, including ferromagnetism, antiferromagnetism, and altermagnetism, are exemplified by Fe, MnPt, and RuO_2. **First row:** Depicts illustrative spin configurations and magnetization densities on crystalline structures in real space. **Second row:** Shows the corresponding band structures and energy iso-surfaces. These reveal ferromagnetically spin-split bands, spin-degenerate bands in the antiferromagnetic phase, and altermagnetic bands, characterized by spin-splitting with opposite signs along different directions in reciprocal momentum space. This figure is modified from Ref. [16].

The spin-split energy isosurfaces in the ferromagnetic phase are isotropic, commonly referred to as *s*-wave Fermi surfaces, though this is an approximation. In contrast, altermagnets exhibit anisotropic spin-split Fermi surfaces [16]. For instance, RuO_2 is classified as a *d*-wave altermagnet due to its specific isosurface geometry, as illustrated in Figure 1.6, where the number of nodes in the isosurface determines this classification. Furthermore, *g*-wave and *i*-wave altermagnets have been identified, with CrSb specifically classified as a *g*-wave altermagnet [8]. The term *altermagnetism* is derived from the alternating spin polarizations observed in both the real-space crystal structure and the reciprocal-space band structure [8]. Altermagnetism is expected to be widespread in nature, occurring in both three-dimensional and two-dimensional crystals, across a variety of structural and chemical types [8]. It spans a wide range of conduction types, including insulators such as Fe_2O_3, semiconductors like

[2]Spin-dependent band splitting in condensed matter systems can also occur due to the relativistic spin-orbit interaction. This is also known as the *Dresselhaus effect* or *Rashba effect* [20, 21]. Especially the latter led to several discoveries and useful applications in spintronics [21].

MnTe, superconductors like La_2CuO_4, and metals such as CrSb [16]. Altermagnetism can also emerge in crystals composed of common light elements and exhibiting high magnetic ordering temperatures, which ensures robust spin coherence and enhances their suitability for device applications [16]. The intrinsic characteristics of altermagnets, such as spin-splitting and vanishing net magnetization, suggest they can combine the advantages of ferromagnets and antiferromagnets within spintronics concepts [16]. For instance, they are expected to enable spin-polarized currents, similar to ferromagnets, potentially resulting in large giant magnetoresistance (GMR) ratios [16]. At the same time, their vanishing net magnetization reduces stray fields, enhancing magnetic robustness akin to antiferromagnets [16]. These unique properties position altermagnets as promising candidates for advancing spintronics research and improving memory device technologies [16]. Notably, the altermagnetic spin-splitting has been experimentally verified in certain materials, such as MnTe [22] and CrSb [23, 24, 25] via angle-resolved photoemission spectroscopy (ARPES).

The spin-splitting of CrSb, as shown in Figure 1.7, is significantly larger than that calculated for most altermagnetic materials, making it a particularly intriguing subject for further investigation. In the following chapters, CrSb will be examined in greater detail with a focus on its crystallographic properties and an in-depth analysis of the material used in magnetotransport experiments.

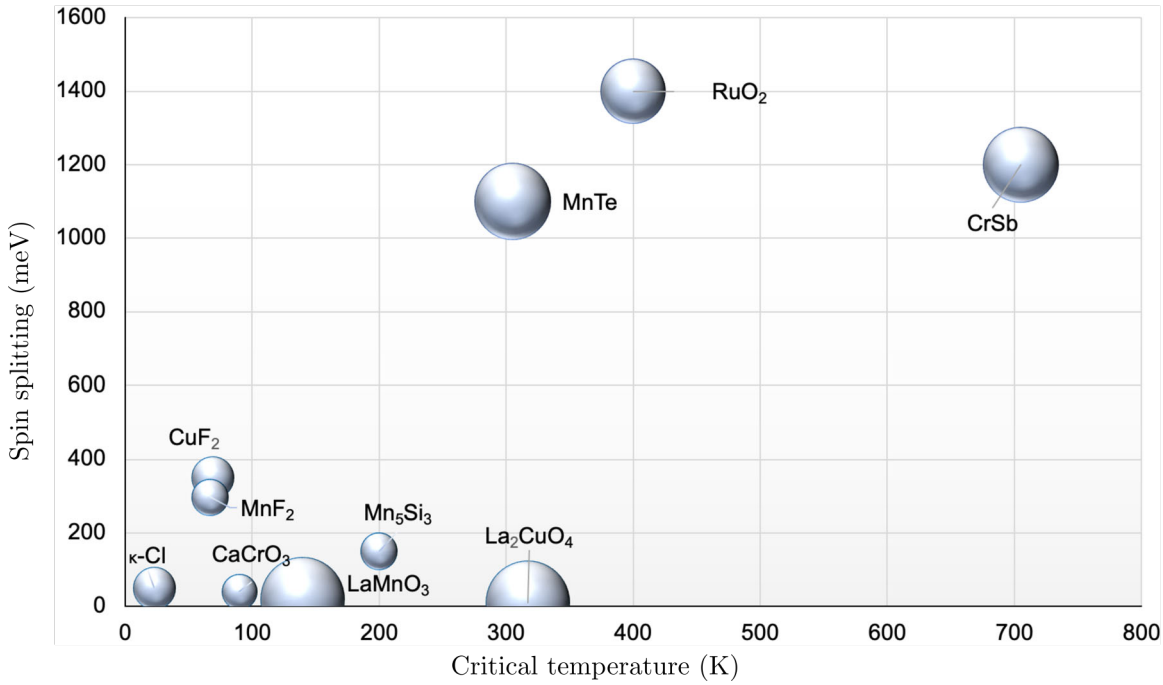

Figure 1.7: Scatter plot of selected altermagnetic candidates from ab initio calculations, showing the Néel or critical temperature along with the spin splitting for each respective compound. The size of the balls is proportional to the largest atomic number in the crystal. This figure is adapted from Ref. [16].

2 Characterization of CrSb

The altermagnetic CrSb crystallizes in the hexagonal NiAs-type structure which refers to the crystal space group $P6_3/mmc$ [26, 27]. The lattice parameters are $a = b = 4.12$ Å and $c = 5.47$ Å. As illustrated in Figure 2.1, the magnetic moments in CrSb are exclusively carried by the chromium sublattices.

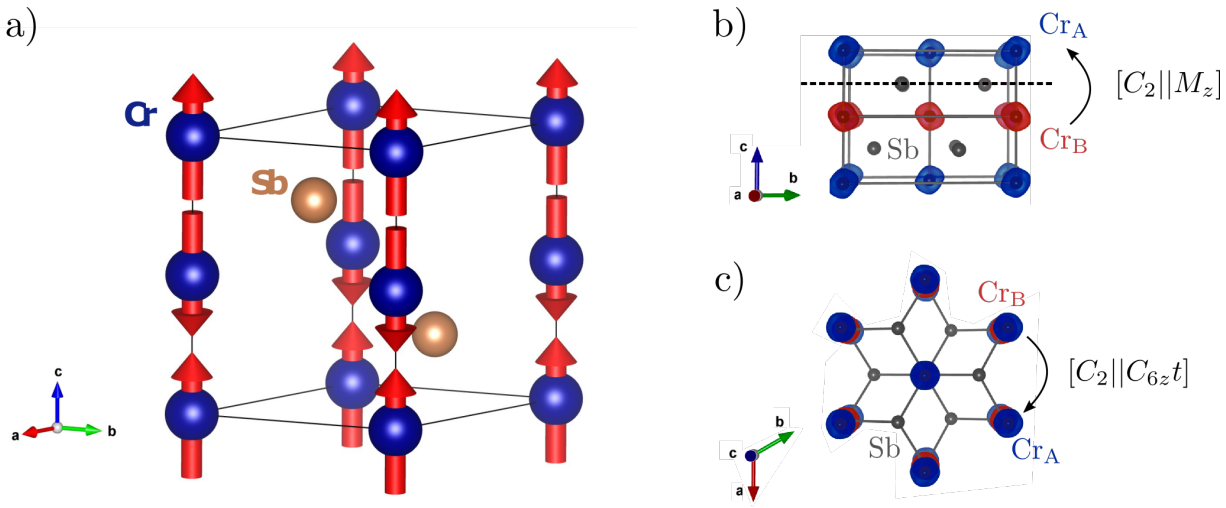

Figure 2.1: a) The hexagonal magnetic unit cell of CrSb. Chromium atoms are represented in blue, while the beige ones correspond to antimony. The magnetic moments of the chromium atoms are directed along the [001] axis or c-axis and parallel aligned in the c-plane, but antiparallel between adjacent c-planes. b) and c) Side and top views of the crystal structure with DFT spin densities, parallel to the a- and c-axes, respectively. The Cr sublattices, with opposite orientation of the magnetic moment, are represented in red and blue. The black arrow and its labels indicate opposite-spin-sublattice transformations. All illustrations were created using VESTA [28], with b) and c) adapted from [8].

The black arrows in panels b) and c) illustrate the symmetric opposite-spin sublattice transformations. These consist of a 180° spin-space rotation around an axis perpendicular to the spins (C_2). In panel b), this transformation is combined with a real-space mirror transformation around the dotted axis (M_z), while in panel c), it is combined with a sixfold real-space rotation and translation ($C_{6z}t$). Note that the index z refers to the c-axis of the hexagonal crystal structure. The crystal potential of antimony induces alternating DFT spin densities in the neighboring chromium sublattices, establishing CrSb as an altermagnet. In Figure 2.2, the band structure calculations along the P-Q-P path in the Brillouin zone are presented. The calculation without spin-orbit coupling reveals a pronounced altermagnetic band splitting, with the spin polarization of the bands reversing sign at the Q-point [23]. When SOC is included, only minor additional band shifts are observed, indicating that SOC does not play a significant role in the formation of the altermagnetic band splitting [23]. The quantum number $\langle S_z \rangle$ provides a clear indication of the band splitting in this collinear system, as it allows only two possible spin states, $+1$ and -1. At the point of maximum band splitting, an arrow is indicated. The nonmagnetic band structure calculations reveal spin-degenerate states. This indicates that the reciprocal energy band splitting in panel c), despite the absence of net magnetization, is evidently driven by crystal fields

[23]. More specifically, the underlying reason is that the chromium atoms in the different sublattices have different DFT spin densities as shown in Figure 2.1, leading to k-dependent energy states. Experimental data from ARPES along the P-Q-P path corroborates the band structure calculations [23]. Furthermore, theoretical predictions suggest substantial altermagnetic spin splitting along the Γ-L path [23].

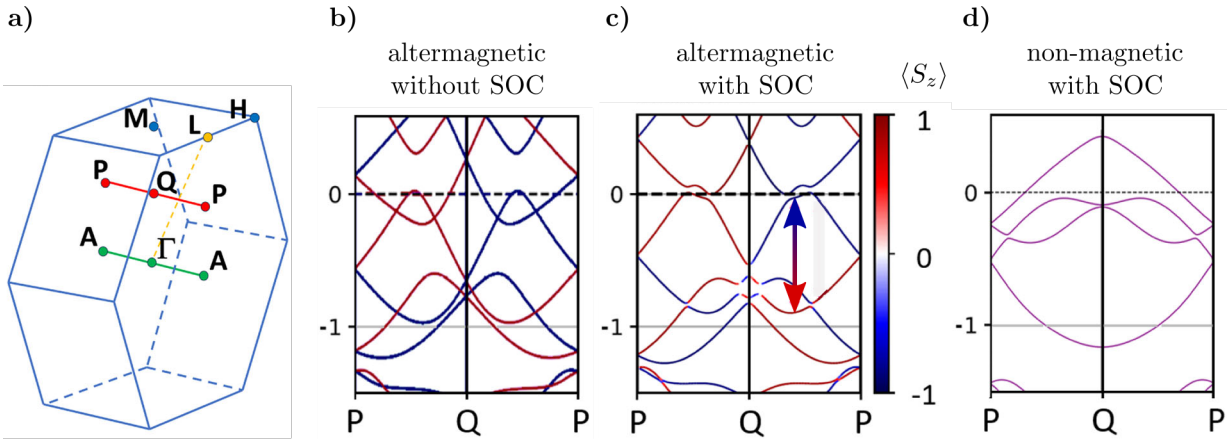

Figure 2.2: a) Brillouin zone of CrSb, highlighting various paths; the calculated band structure along the P-Q-P path is depicted in b) altermagnetic without SOC, c) altermagnetic with SOC, and d) nonmagnetic with SOC. The color of the bands in b) and c) indicates the spin polarization. This figure is adapted from Ref. [23]

Notably, each chromium ion carries a magnetic moment of $3.0\,\mu_B$ at 0 K [29]. The Néel temperature of the compound has been determined to be 705 K [29], ensuring magnetic ordering persists well above room temperature, making it suitable for practical applications. In the following, some bulk and thin film samples are examined for their magnetic and crystallographic attributes to confirm the presence of the altermagnetic CrSb, which is the focus of our magnetotransport studies.

2.1 Bulk

The bulk material utilized in this study consists of high-quality *single crystals*, synthesized via chemical vapor transport reactions (CVT). In this crystallization method, the starting materials (source) and a gaseous transport agent are sealed within a transport ampoule, which is subjected to a temperature gradient between its two ends [30]. The temperature gradient induces a circulation of the gas, which reacts with the source material and transports the resulting volatile compounds to the cooler region of the ampoule, where the gas mixture resublimates and the crystal growth occurs [30]. By adjusting parameters such as the internal pressure of the ampoule, the temperature gradient, and the length of the diffusion path, the crystallization process can be fine-tuned to achieve the desired crystal structure [30]. The crystals shown in Figure 2.3 exhibit similar dimensions. Their average thickness is approximately 2 mm, with widths ranging from 2 to 3 mm, and lengths varying between 3 and 9 mm.

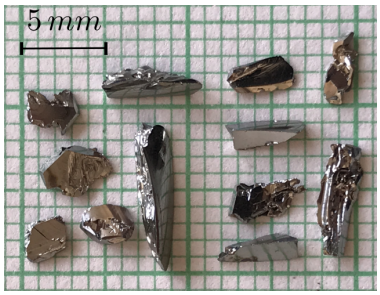

Figure 2.3: A selection of CrSb single crystals, grown in the same batch using the CVT method by Jiří Pospíšil.

While the majority of the crystals lack a well-defined morphology, a subset exhibits flat and smooth surfaces. A few of these crystals are characterized by two parallel flat faces, while the remaining edges have a more irregular, "potato"-like contour. Additionally, the crystals exhibit a metallic grayish luster, contributing to their overall shiny appearance. The crystals are quite brittle and exhibit a tendency to fracture along specific cleavage planes. To demonstrate the quality of the crystals following measurements provide information about the material used in magneto transport measurements in Chapter 4. The Laue pattern in Figure 2.4 shows a sixfold symmetry which means that the incoming beam is perpendicular to the (001) plane from the hexagonal CrSb structure.

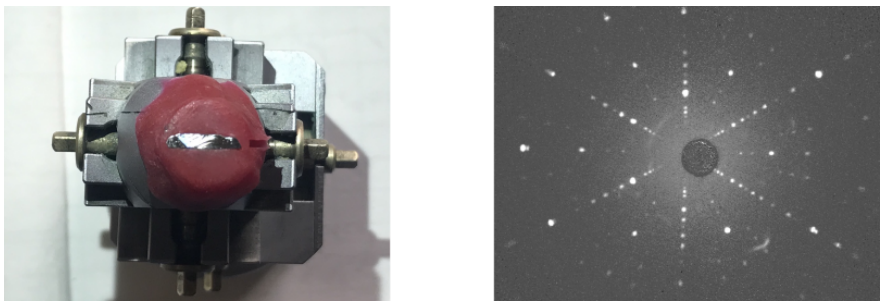

Figure 2.4: **Left:** An atypical elongated crystal featuring a flat and smooth surface, positioned on a sample holder for Laue diffraction. **Right:** Backscattered Laue diffraction pattern obtained from the crystal depicted in the left image at room temperature.

The same measurement was repeated on various spots on the same crystal with consistent result. For crystals without a flat surface, the Laue patterns did not exhibit clear sixfold symmetry. Therefore, it is logical to focus on crystals with flat surfaces for analysis. In Figure 2.5, a 2θ scan of powder prepared from a single crystal is displayed, showcasing the diffraction pattern. The excellent alignment between the experimental data and the simulated intensities verifies the sample's phase purity, confirming the exclusive presence of CrSb in the NiAs phase. This alignment further indicates the accuracy of the synthesis method used for this samples.

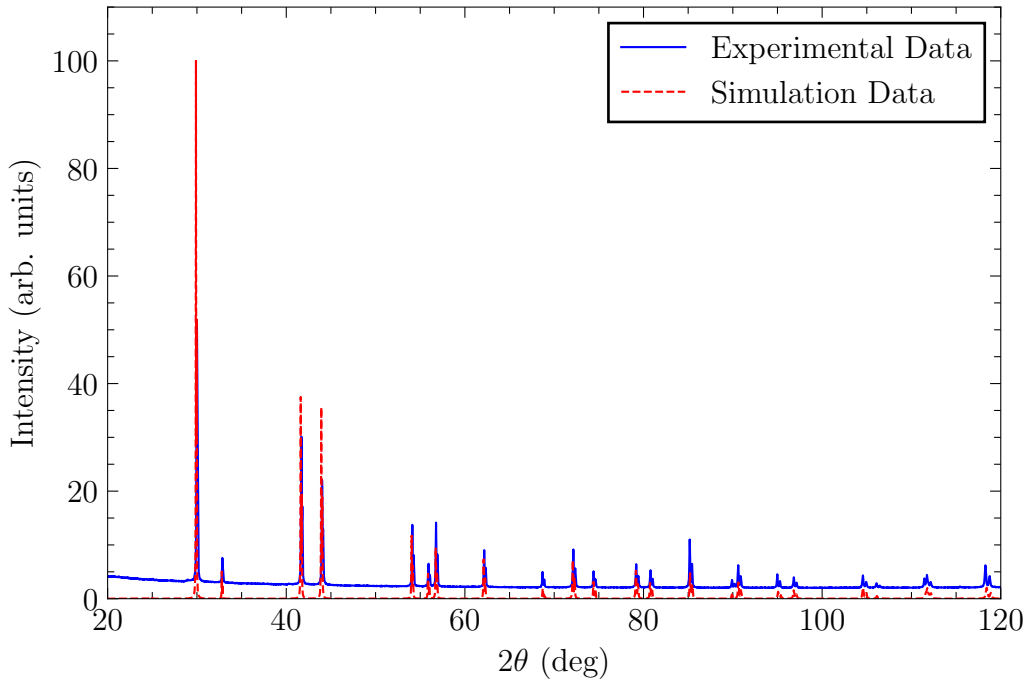

Figure 2.5: Powder diffraction pattern of CrSb. The blue line represents the experimentally measured data from a single crystal, while the red-dotted line shows the simulated intensity values derived using VESTA software [28].

Figure 2.6 shows the dependence of magnetization on external magnetic field for $\mu_0 H \perp c$ and $\mu_0 H \parallel c$ at 5 K using a superconducting quantum interference device (SQUID) from Quantum Design. The magnetization is reported in units of μ_B per formula unit, which in this context corresponds to the magnetic contribution per chromium atom, as the magnetic behavior originates from the chromium atoms only, as illustrated in Figure 2.1. For both field orientations, the magnetization exhibits a linear dependence on the applied field, with no observable hysteresis — a characteristic consistent with a compensated magnetic system. Additionally, the zero magnetization at zero field further supports the presence of compensated ordering. It is also noteworthy that the slope of the green line ($\mu_0 H \parallel c$) is less steep than that of the purple line ($\mu_0 H \perp c$), aligning with the expected anisotropic behavior of the system. This indicates that the magnetic susceptibility χ is greater when the field is applied perpendicular to the magnetic easy axis of CrSb than when it is applied parallel to it, which is consistent with the discussion in Section 1.2.

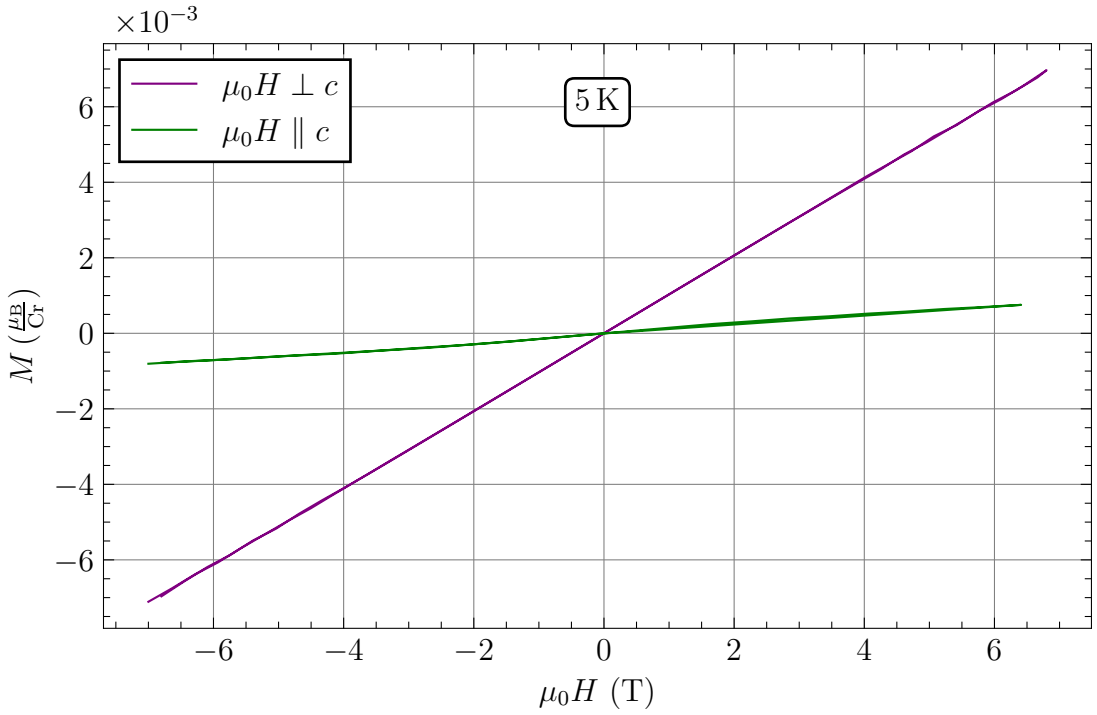

Figure 2.6: Magnetization as a function of magnetic field, measured for two different field orientations with a SQUID. The purple curve represents the orientation in which the magnetic field is applied perpendicular to the easy axis, while the green curve corresponds to the field orientation parallel to the easy axis. Both measurements were performed at 5 K.

This magnetometric result is significant as it verifies the presence of the compensated NiAs phase of CrSb, which is crucial because an alternative form of CrSb exists with properties distinct from the altermagnetic CrSb. Specifically, CrSb in the zincblende structure demonstrates ferromagnetic behavior at room temperature [31]. Moreover, there is no indication of a spin-flop or spin-flip transition within the measured field range. Applying equation (12) from the Stoner-Wohlfarth model, combined with ab initio calculations for the exchange coupling and magnetocrystalline anisotropy of CrSb, one obtains

$$B_{sf} = 2\sqrt{B_a B_{ex}} > 300\,\mathrm{T}. \tag{13}$$

It is also apparent that, even at the maximum applied field of ±7 T, the magnetic moments remain on the order of $10^{-3}\,\mu_B$, which is significantly smaller than the $3\,\mu_B$ of a single chromium atom. This indicates that the spins of the respective sublattices are strongly coupled, with only minimal canting towards the field direction.

2.2 Thin Films

The previously described bulk samples are not suitable for technical applications due to their size. Consequently, thin films are of greater interest for microelectronics research and applications. However, intrinsic magnetic properties such as magnetization, Curie temperature, and anisotropy can vary significantly between bulk materials and thin films [9]. This difference can be attributed to the fact that atoms at the surface of a thin film have fewer nearest neighbors compared to atoms in the bulk material [10]. As a result, the electronic bandwidth is reduced, while the density of states at the Fermi level ($DOS(E_F)$) increases simultaneously [10]. This enhances the likelihood of satisfying the Stoner criterion (equation (8)), leading to a stronger tendency toward magnetic ordering [10]. Consequently, one would expect enhanced magnetic moments in thin films compared to bulk materials [10]. Additionally, these variations can be influenced by surface or interface effects, as well as strain induced by the film's substrate, which can further cause deviations in lattice parameters from those observed in the bulk [9]. In order to grow an *epitaxial* single-crystal thin film it is crucial to choose a substrate with minimal lattice mismatch. For CrSb, it turned out that in our process, the only way to obtain it in the desired orientation and epitaxial is to grow it on top of an insulating SrF_2 (111) substrate with an additional layer in between, namely PtSb (001). This nonmagnetic metal readily grows directly on the substrate and serves as a buffer to stabilize epitaxial (001) CrSb films. In our case, all previous attempts on growing CrSb alone showed polycrystalline growth. The in-plane lattice mismatch of the a - and b - axis of PtSb and CrSb is zero ($a = b = 4.12$ Å), while the mismatch between the substrate and the PtSb layer is 0.5 %. The multilayer PtSb/CrSb thin film with the thicknesses 30 nm and 20 nm in Figure 2.7 was grown via direct current (dc) magnetron co-sputtering, a thin-film deposition technique where the target materials (Cr, Pt, and Sb) are bombarded by ions in a plasma, causing atoms to be ejected and deposited on a substrate. The use of a magnetic field helps confine electrons near the target, enhancing ionization and improving deposition efficiency [32]. All thin film samples occurring in this work were grown by Satya Prakash Bommanaboyena.

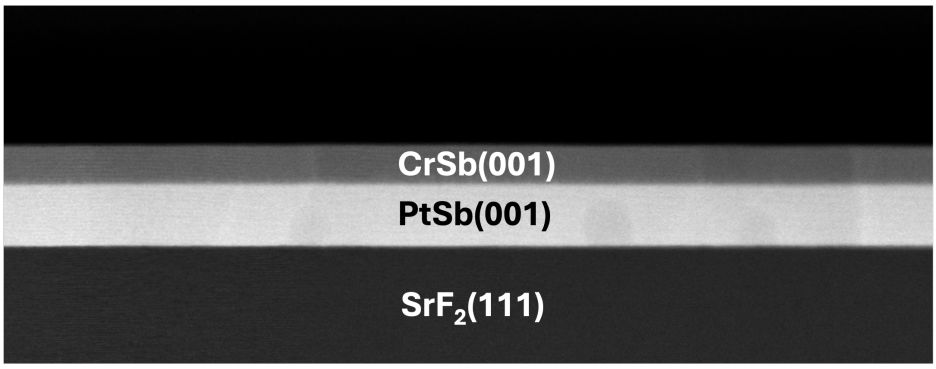

Figure 2.7: High-angle annular dark-field (HAADF) image from the cross section of a PtSb/CrSb multilayer film taken by a scanning transmission electron microscope (STEM). The viewing direction is the $[2\bar{1}0]$ direction of CrSb and PtSb. This image was taken by Filip Křížek.

In Figure 2.8 and 2.9, the interfaces between the SrF_2 substrate and the PtSb buffer layer, as well as between the PtSb buffer layer and CrSb, are depicted in greater detail. The smoothness of the interfaces indicates high quality and defect free epitaxial growth of the multilayer film.

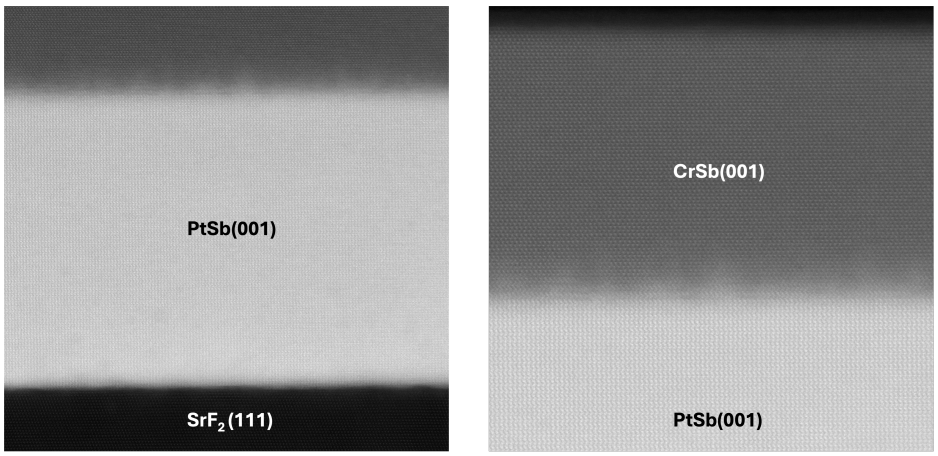

Figure 2.8: Close up pictures from Figure 2.7. **Left:** Interface between the SrF_2 substrate and the PtSb (001) buffer layer. **Right:** Interface between the PtSb (001) buffer layer and the CrSb (001) layer. This image was taken by Filip Křížek.

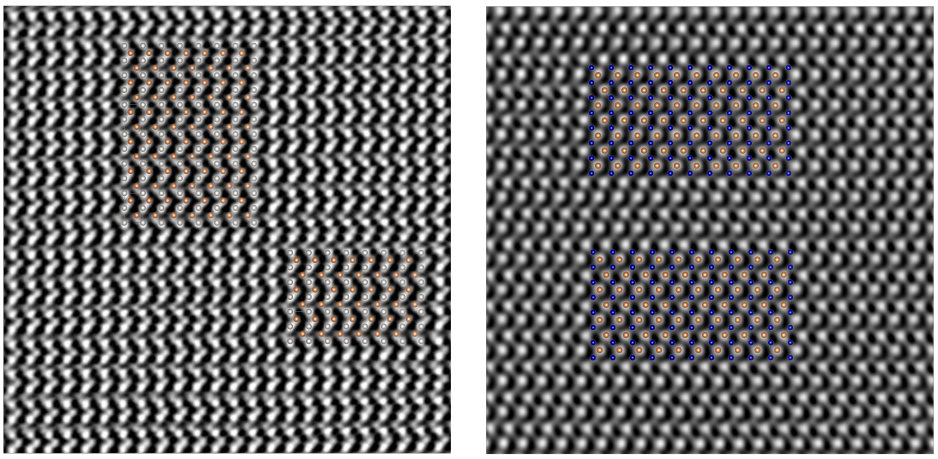

Figure 2.9: Close up pictures from Figure 2.7. **Left:** PtSb (001) layer. **Right:** CrSb (001) layer. In each image, the crystal structure of the compounds along this direction is illustrated, demonstrating an excellent match with the microscopic picture. The orange spheres depict Sb atoms, the gray ones correspond to Pt atoms, and the blue ones indicate Cr atoms. This image was taken by Filip Křížek.

X-ray diffraction (XRD) measurements were carried out to confirm the crystallographic structure and orientation of our PtSb/CrSb thin film sample with a Rigaku Smartlab diffractometer in the parallel beam configuration using Cu-Kα_1 radiation. Figure 2.10 shows a radial scan of the multilayer sample *CS240805A* which will also be discussed in Chapter 4. The thicknesses of this sample are 15 nm (PtSb) and 25 nm (CrSb). The sharp peaks at 26.6° and 54.78° can be assigned to the (111) and (222) plane of the substrate SrF_2, while the peaks at 32.7° and 68.7° represent the desired (002) and (004) planes of PtSb/CrSb. Both peaks show multiple orders of Laue oscillations, implying a very high degree of crystallinity [33]. Using the peak simulations in the kinematic model of diffraction, the lattice constants of $c = 5.50$ Å (PtSb) and $c = 5.49$ Å (CrSb) are extracted which is in excellent agreement with the values reported earlier for the two compounds. The lattice constant of $a = 4.12$ Å for both layers was determined from a reciprocal space map, aligning perfectly with the theoretical value. The absence of any other peaks reveals the single crystalline growth and, hence, an excellent sample quality.

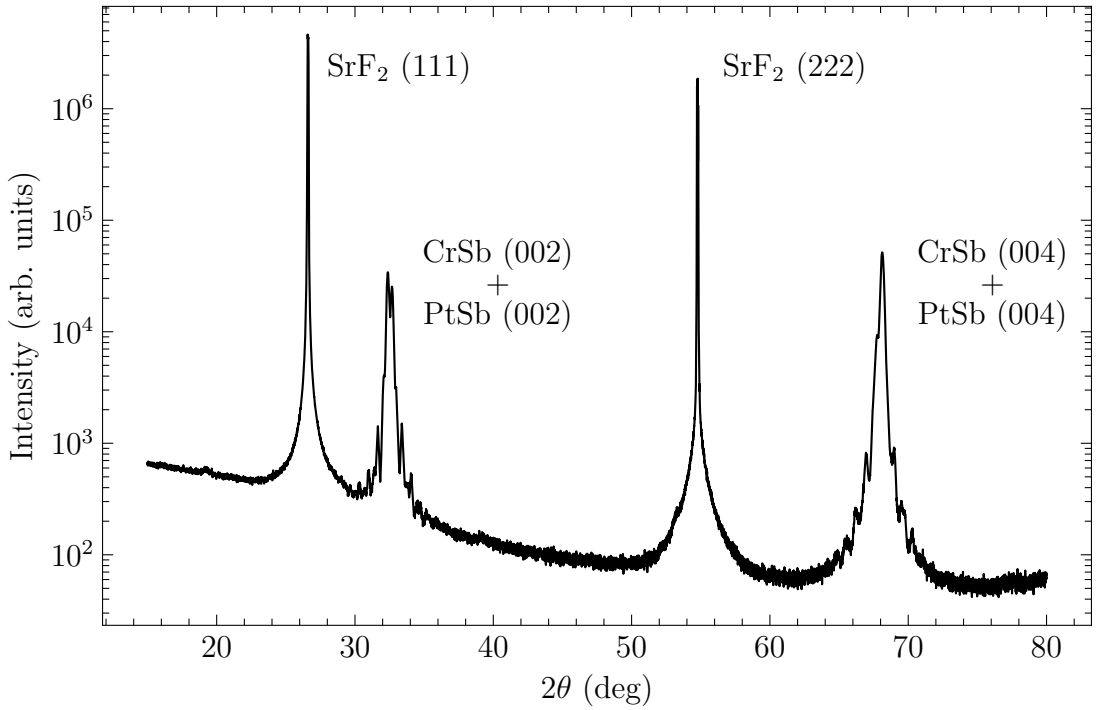

Figure 2.10: XRD radial scan of the sample *CS240805A*.

A pole figure was measured for the $\{1\bar{1}2\}$ or r-planes of the PtSb/CrSb structure to determine its in-plane orientation and confirm the sixfold rotational symmetry of the hexagonal crystal structure. Six $\{1\bar{1}2\}$ poles (or diffraction maxima), circled in red, are observed at $\chi \approx 38°$ (sample tilt) with a periodicity of 60° in ϕ (sample azimuth). The equidistance of the poles affirms the perfect sixfold symmetry of the (001)-oriented hexagonal unit cells of both layers. The relevant in-plane crystallographic directions were also determined based on the pole positions in ϕ which will be relevant for the measurements in Chapter 4.

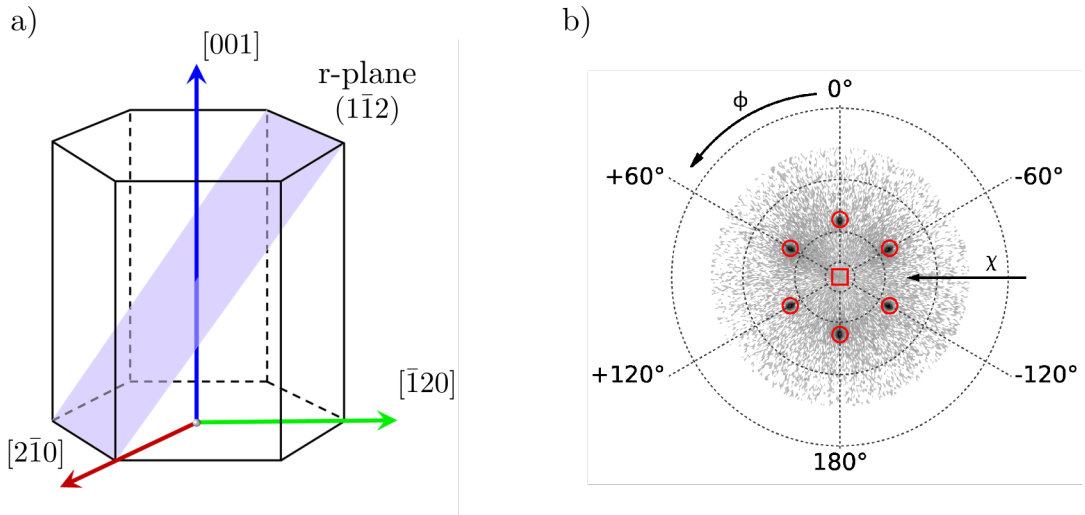

Figure 2.11: a) Hexagonal crystal directions along with the r-plane. b) Pole figure for $\{1\bar{1}2\}$ or r-planes of the sample *CS240805A* (stereographic projection). The sample was aligned such that $SrF_2[1\bar{1}0]$ was parallel to the diffraction plane at $\phi = 0°$.

3 Theoretical Background of Magnetotransport

By investigating phenomena that arise from the transport of electric charge (such as electrons and holes) in solids, various material properties can be determined. By applying an external magnetic field, numerous additional field-dependent properties can be observed and characterized. The following sections provide a concise introduction to the fundamental concepts of electrical transport, emphasizing its dependence on magnetic fields. Key principles such as resistivity, conductivity, and their tensorial nature in the presence of magnetic fields will be discussed to establish a foundation for understanding the observed phenomena.

3.1 Conductivity in the Drude Model and Magnetoresistance

To analyze the mechanisms underlying electrical conduction, Paul Drude introduced the *Drude model* at the turn of the 20th century. A central postulate of this model is the representation of electrons as small, particle-like entities moving through a lattice structure composed of relatively immobile, heavy core ions. The interactions or scattering events between these stationary atomic cores and the mobile electrons serve to explain the resistance encountered in conductors. While fundamentally classical in nature — and thus limited in accuracy within the quantum mechanical framework — the Drude model remains instrumental for a qualitative understanding of solid-state behavior. A primary outcome of the Drude model is the derivation of Ohm's law, expressed as

$$\vec{j} = \sigma \vec{E} \tag{14}$$

where $\vec{j}$ denotes the current density induced by the electric field $\vec{E}$ [34]. Here, the term $\sigma = nq\mu$, defined as the *electrical conductivity*, depends on the electron density n, the charge q, and the electron mobility μ. The inverse of conductivity is referred to as *resistivity*, given by:

$$\rho = \sigma^{-1}. \tag{15}$$

Note that, in the general case, conductivity and resistivity must be treated as three-dimensional tensors, expressed as:

$$\rho = \begin{pmatrix} \rho_{xx} & \rho_{xy} & \rho_{xz} \\ \rho_{yx} & \rho_{yy} & \rho_{yz} \\ \rho_{zx} & \rho_{zy} & \rho_{zz} \end{pmatrix}. \tag{16}$$

Thin-film analysis effectively uses a two-dimensional tensor, while bulk transport neglects z-direction currents due to the samples' plate-like geometry. Experimentally determining the material-specific resistivity involves using the expression

$$\rho = R\frac{A}{l}, \tag{17}$$

which indicates that resistivity is proportional to the *electrical resistance* R, the cross-sectional area A, and the distance l between the contacts on the sample. In general, A is the product of the width w and the thickness t of the sample. Note that, in the case of the transverse resistivity, the width of the contacts is equal to the separation between them. This distinction leads to:

$$\rho_{xx} = R\frac{wt}{l} \quad \text{and} \quad \rho_{yx} = Rt. \tag{18}$$

In the case of a conductor with a single type of charge carrier moving at velocity v under the influence of an applied electric field $\vec{E}$, the carriers are subject to additional effects from an externally applied magnetic field, specifically experiencing the *Lorentz force*:

$$\vec{F_L} = q(\vec{v} \times \vec{B}). \tag{19}$$

This interaction generates an electric field $\vec{E_H}$ that compensates for the influence of the Lorentz force F_L, leading to the condition:

$$e(\vec{E_H} + \vec{v} \times \vec{B}) = \vec{0}. \tag{20}$$

By defining the applied electric current moving only in the x-direction ($\vec{v} = (v_x, 0, 0)$) and the magnetic field as $\vec{B} = (0, 0, B_z)$ — thus perpendicular to the motion of the charge carriers — the y-component of equation (20) is obtained as

$$E_{H_y} - v_x B_z = 0. \tag{21}$$

Using the relation $\vec{j} = nq\vec{v}$, this yields $E_{H_y} = \dfrac{j_x B_z}{nq}$. Additionally, applying Ohm's law, the transverse resistivity can be determined as:

$$\rho_{yx} = \frac{B_z}{nq} \tag{22}$$

which is known as the *ordinary Hall effect* (OHE) [35]. This relation demonstrates that, with the application of a magnetic field, the transverse resistance increases linearly with the field strength, making the Hall effect an odd function of the magnetic field. The longitudinal resistance ρ_{xx} however, is not influenced by the Lorentz force, as the x-component of equation (20) is not dependent on B. This indicates that the *ordinary magnetoresistance* (OMR), defined as

$$\text{OMR} = \frac{\rho_{xx}(B) - \rho_{xx}(B = 0)}{\rho_{xx}(B = 0)} \tag{23}$$

is strictly zero under the assumption of single-band, single-carrier transport. In general, the OMR is significantly influenced by temperature. At lower temperatures, magnetoresistance becomes more significant due to reduced thermal phonon scattering [36].

From equations (19) and (20), the two-dimensional conductivity tensor in the presence of a magnetic field can be derived as:

$$\sigma = \begin{pmatrix} \sigma_{xx} & \sigma_{xy} \\ \sigma_{yx} & \sigma_{yy} \end{pmatrix} = \frac{nq\mu}{1 + (\mu B)^2} \begin{pmatrix} 1 & -\mu B \\ \mu B & 1 \end{pmatrix}. \tag{24}$$

Interestingly, although ρ_{xx} is field-independent, σ_{xx} exhibits field dependence.

There exist several additional magnetoresistance phenomena, such as *anisotropic magnetoresistance* (AMR), *giant magnetoresistance* (GMR), and *tunneling magnetoresistance* (TMR). However, these effects will not be elaborated upon here, as their manifestation depends on magnetic properties that are absent in the material studied in this work, and they are therefore not anticipated in the experimental results presented in the following chapter. It is nevertheless noteworthy that the discovery of the GMR effect is regarded as marking the advent of spintronics [37].

3.2 Multiband Magnetoresistance

In reality, the conductivity of a material can arise from mixed contributions of electron- and hole-like carriers. This also includes the possibility of having two distinct contributions to the conductivity arising from electron bands with different carrier densities and mobilities. For instance, in intrinsic semiconductors at $T > 0$, the conduction band is sparsely populated with electron-like carriers, while the valence band hosts hole-like carriers with lower mobility [13]. It is important to note that fully filled bands do not contribute to charge transport. When interpreting the measured Hall voltage arising from both electrons and holes, compensation effects may arise [13]. This is because electrons and holes are deflected to the same side of the sample [13]. Interpreting the measured Hall data using the single-band model may result in an unreasonably high carrier density [13]. To account for the mixed carrier contributions, the single-band conductivity tensor in equation (24) must be generalized for an individual band i under $\vec{B}||\hat{z}$:

$$\sigma_i = \frac{n_i q \mu_i}{1 + (\mu_i B)^2} \begin{pmatrix} 1 & -\mu_i B \\ \mu_i B & 1 \end{pmatrix}. \tag{25}$$

Note that at this point it is important to consider that the sign of the charge q differs between electrons and holes. In the following, the charge of electrons will be defined as $e \approx -1.602 \times 10^{-19}$ C, while the charge of holes will be set to $-e$. It is also important to note that the sign of the carrier densities n_i and mobilities μ_i is always considered to be positive. The total conductivity is then obtained by summing the contributions from all bands:

$$\sigma = \sum_{i=1}^{N} \sigma_i. \tag{26}$$

The corresponding resistivity tensor can be derived once the conductivity is determined using equation (26). For the case of $N = 1$ assuming electron transport, this leads to:

$$\rho_{xx}(B) = \frac{1}{ne\mu} \quad \text{and} \quad \rho_{yx}(B) = -\frac{B}{ne} \tag{27}$$

as described in the previous section. For $N = 2$ we have the *two band model* and we get

$$\rho_{xx}(B) = \frac{1}{e} \frac{(n_e\mu_e + n_h\mu_h) + (n_e\mu_e\mu_h^2 + n_h\mu_h\mu_e^2)B^2}{(n_e\mu_e + n_h\mu_h)^2 + (n_e - n_h)^2\mu_e^2\mu_h^2B^2} \tag{28}$$

and

$$\rho_{yx}(B) = \frac{1}{e} \frac{(n_e\mu_e^2 - n_h\mu_h^2) + (n_e - n_h)\mu_e^2\mu_h^2B^2}{(n_e\mu_e + n_h\mu_h)^2 + (n_e - n_h)^2\mu_e^2\mu_h^2B^2} B. \tag{29}$$

At this stage, we consider the electron density (n_e), hole density (n_h), and the respective mobilities of electrons (μ_e) and holes (μ_h). With each additional band, two more parameters are introduced that influence the resistivity of a material. Unlike the single-band model, the longitudinal resistivity $\rho_{xx}(B)$ becomes field-dependent for $N \geq 2$ and typically exhibits a behavior reminiscent of a quadratic dependence on B.

3.3 Mobility Spectrum Analysis

In the previously discussed multiband approach to explain transport behavior in the presence of a magnetic field, equation (25) assumes a discrete spectrum of carrier mobilities, where each type of carrier is assigned a distinct scalar μ_i. In Ref. [38], the authors demonstrated that, for a wide range of cases, the field-dependent conductivity in a material can be described in terms of a continuous mobility spectrum. This means that from equation (25), $n_i q \mu_i = \sigma_0^{(i)} \rightarrow \sigma_0(\mu)$, where each value of μ corresponds to a certain carrier density assigned to this mobility. Simultaneously, the concept behind the presented mobility spectrum analysis (MSA) is that, as the number of bands N in equation (26) approaches infinity ($N \rightarrow \infty$), the sum is replaced by an integral over μ [39]. The longitudinal and transverse conductivity in the presence of a magnetic field along $\hat{z}$ are then:

$$\sigma_{xx} = \int_{-\infty}^{\infty} \frac{\sigma_0(\mu) d\mu}{1 + (\mu B)^2} \tag{30}$$

and

$$\sigma_{yx} = \int_{-\infty}^{\infty} \frac{\mu B \sigma_0(\mu) d\mu}{1 + (\mu B)^2}. \tag{31}$$

Note that in this convention, the sign of the mobilities for electrons and holes are of opposite signs, as $\sigma_0(\mu)$ must be ≥ 0 for a physical spectrum [39]. The key aspect of the MSA is now to calculate $\sigma_0(\mu)$ from the measured $\sigma_{xx}(B)$ and $\sigma_{yx}(B)$ at a finite number of magnetic fields [39]. The methods for this calculation shall not be discussed in this work, but they can be found in Ref. [39]. The mobility spectrum analysis will be applied in the following chapter to the measured bulk data to compare resistivities derived from MSA with those obtained from multiband fittings.

4 Magnetotransport Properties of CrSb

4.1 Experimental Setup

To maintain consistency in the following discussion, the coordinate system is defined as illustrated in Figure 4.1.

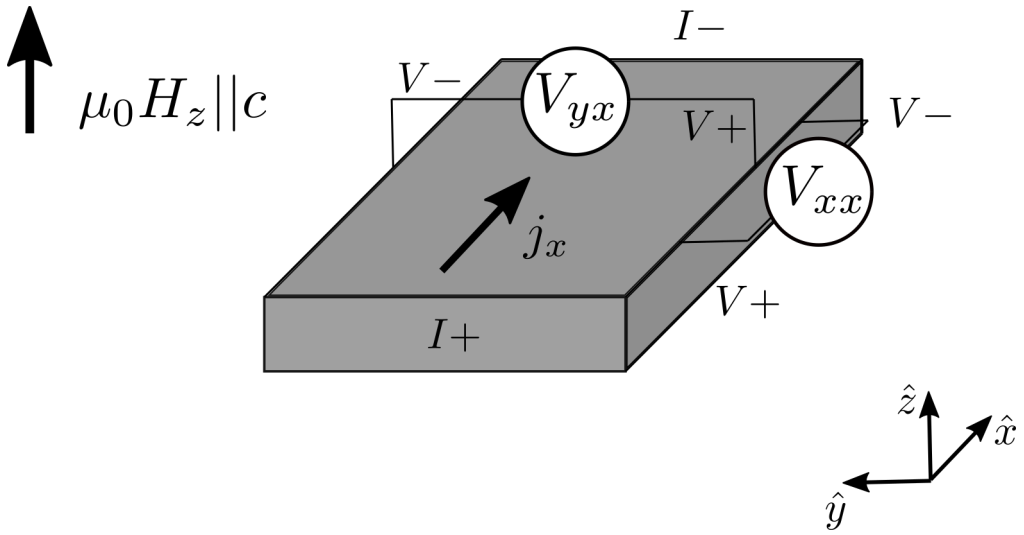

Figure 4.1: Schematic experimental setup using the conventional four-terminal method. The polarity of the Hall voltage is crucial for determining the type of carriers, as it is influenced by the Lorentz force, which in turn depends on the sign of the charge.

As discussed in the previous chapter the definition of the measured resistivity starts with Ohm's law $\vec{j} = \vec{\sigma} \cdot \vec{E}$ or $\vec{E} = \vec{\rho} \cdot \vec{j}$ in the two dimensional tensor form

$$\begin{pmatrix} E_x \\ E_y \end{pmatrix} = \begin{pmatrix} \rho_{xx} & \rho_{xy} \\ \rho_{yx} & \rho_{yy} \end{pmatrix} \begin{pmatrix} j_x \\ j_y \end{pmatrix} \tag{32}$$

while the external field is applied in $\hat{z}$-direction. As current is sent in x - direction ($j_y = 0$) and the voltage drop measured along the x - direction (longitudinal) and y - direction (transversal) we end up with

$$\begin{pmatrix} E_x \\ E_y \end{pmatrix} = \begin{pmatrix} \rho_{xx} \cdot j_x \\ \rho_{yx} \cdot j_x \end{pmatrix}. \tag{33}$$

The respective measured voltage drop is proportional to the electric field and the distance d of the contacts, as per the relation $V = E \cdot d$. The magnetic field is intentional aligned parallel to the c-axis of CrSb in both the bulk and thin film samples to investigate the potential occurrence of the spin-flop or spin-flip phenomenon, as discussed in Section 1.2. All following magnetotransport properties were measured with a physical property measurement system (PPMS) from Quantum Design. The current used in the PPMS is an alternating current (AC). The longitudinal resistivity obtained from the measurements, ($\rho_{xx}^{meas}(\mu_0 H_z)$), was symmetrized with respect to the external applied magnetic field $\mu_0 H_z$, while the Hall resistivity ($\rho_{yx}^{meas}(\mu_0 H_z)$) was anti-symmetrized. The reason for this is that geometric irregularities in the sample's shape or the positioning of the contacts, which can introduce additional contributions and artifacts to the resistivity measurements, are effectively eliminated.

Mathematically, the data are processed as follows:

$$\rho_{xx}^{sym}(\mu_0 H_z \downarrow) = \frac{\rho_{xx}^{meas}(\mu_0 H_z \downarrow) + \rho_{xx}^{meas}(-\mu_0 H_z \uparrow)}{2} \tag{34}$$

and

$$\rho_{yx}^{asym}(\mu_0 H_z \downarrow) = \frac{\rho_{yx}^{meas}(\mu_0 H_z \downarrow) - \rho_{yx}^{meas}(-\mu_0 H_z \uparrow)}{2}, \tag{35}$$

where $\downarrow$ indicates the corresponding sweep direction from maximum positive field to maximum negative and vice versa with $\uparrow$. To obtain ρ_{xx} and ρ_{yx}, the associated $\rho_{xx}^{sym}(\mu_0 H_z \uparrow)$ and $\rho_{yx}^{asym}(\mu_0 H_z \uparrow)$ can be derived by interchanging the two terms in the numerator of equations (34) and (35). The impact of separating the odd and even components of the measured data can be seen in Figure 4.2.

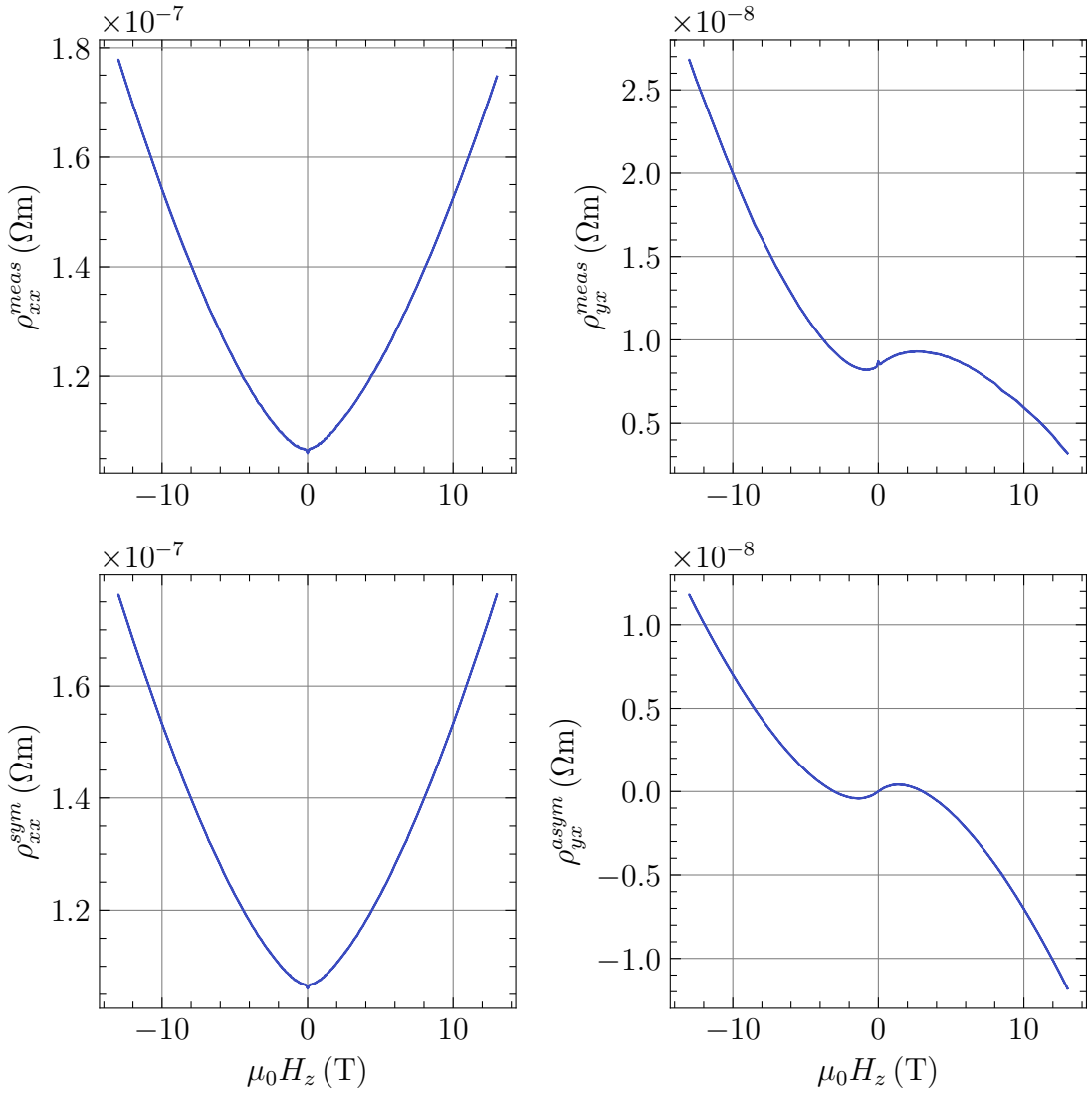

Figure 4.2: **Top:** Exemplary measured longitudinal (left) and transverse (right) resistivity. **Bottom:** Data from the top row after isolating the even (left) and odd (right) components with respect to the applied magnetic field.

The measured longitudinal resistivity remains almost unchanged, whereas the Hall resistivity shows a definite change. In the raw measurement, there is no sign change in ρ_{yx}. After eliminating the even contribution, we observe that at zero field, the Hall resistivity is zero, as expected, since at zero field there is no Lorentz force to induce a Hall voltage. This indicates that some contributions from the longitudinal resistivity are present in the raw data of the transverse resistivity, which are successfully removed by the antisymmetrization. It is important to clarify that the property directly measured in the PPMS is the resistance R. To obtain the more practical and comparable quantity, the resistivity ρ, the specimen's volume is considered as shown in equation (17). The unit of resistance R is ohms (Ω), while the SI unit of resistivity ρ is ohm-meter (Ωm).

4.2 Magnetotransport in Bulk

To perform magnetotransport measurements in bulk crystals, as shown in Figure 2.3, it is crucial to select crystals with an appropriate geometry. As previously described, our focus is on magnetoresistance under an external magnetic field applied parallel to the c-axis of CrSb. Consequently, it is necessary to choose a crystal with a flat surface. Laue diffraction measurements revealed that cuboid-shaped crystals with flat surfaces have their largest surfaces aligned parallel to the hexagonal (001) plane. The sample depicted in Figure 4.3 is the same as that shown in Figure 2.4, confirming that the out-of-plane direction is the [001] orientation. Additionally, based on simulations of Laue crystallographic data, it is established that the long edge of the sample aligns with the [110] direction of CrSb.

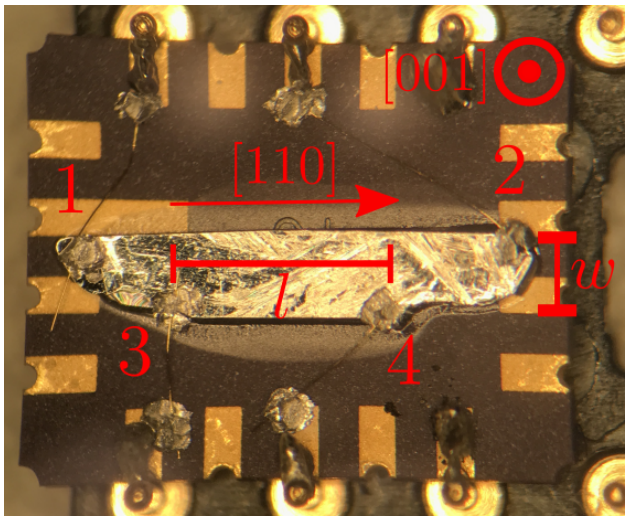

Figure 4.3: Experimental setup for a typical bulk transport measurement performed for this work.

The sample was attached to an eight-contact chip carrier using non-conductive polymethylmethacrylate (PMMA). The contacts on the sample were established using the *indium pressing* technique. This method leverages the malleability of indium to form a "sandwich" consisting of two small pieces of indium with a gold wire placed between them. The contact-resistance is typically in the order of 1 Ω. Contacts 1 and 2 are positioned at the far left and right ends of the sample to apply an electric field and induce a current along the [110] direction. Contacts 3 and 4 are placed to measure the longitudinal resistance over a distance of $l = 3.5$ mm. The cross-sectional area through which the current flows is defined by the sample's width, $w = 1.5$ mm, and thickness, $t \approx 0.5$ mm. The applied current in all bulk measurements was 10 mA which refers to a current density of $j \approx 1.33 \times 10^4$ A/m^2.

The first type of transport measurement is a temperature sweep of the longitudinal resistance to verify the purity of our material, or more precisely, to investigate the *residual-resistance ratio* (RRR), which is usually defined as the ratio of the resistance of a material at room temperature and at a very low temperature [40]. Because we cannot reach 0 K in any experiment, we define the RRR as

$$\mathrm{RRR} = \frac{R_{300K}}{R_{5K}}. \tag{36}$$

A high RRR value indicates a low concentration of impurities and crystallographic defects within the material [40]. Since this quantity is unitless, it is irrelevant whether we take the ratio of resistance or resistivity. For highly pure metals, the RRR value can reach an order of magnitude 10^3 (e.g., in copper and gold) [41], whereas in alloys, it is typically RRR ≈ 1 [13]. Figure 4.4 displays the longitudinal resistance and resistivity from a temperature sweep of a CrSb bulk sample, along with its RRR.

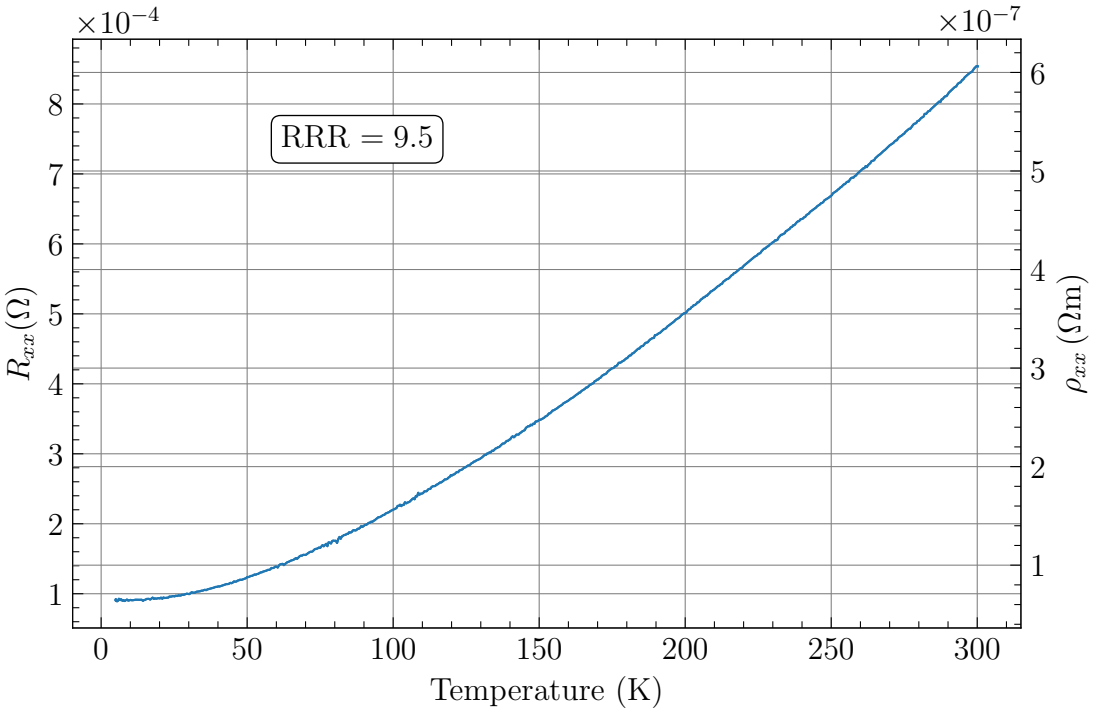

Figure 4.4: Temperature dependence of longitudinal resistance R_{xx} (left scale) and resistivity ρ_{xx} (right scale).

The qualitative temperature dependence of the resistivity exhibits the characteristic behavior expected for a metallic material, affirming that the compound can be classified as metal-like. In the expression

$$\rho_{xx} = \frac{1}{\sigma_{xx}} = \frac{1}{ne\mu} = \frac{m}{ne^2\tau} \tag{37}$$

the only temperature-dependent variable in metals is typically the scattering time τ, where m represents the mass of the charge carrier [13]. The primary mechanisms affecting the residual-resistance ratio are electron scattering by phonons, defects, impurities, and surface interactions [13]. At lower temperatures (5 K - 20 K), scattering due to impurities and defects dominates [42], resulting in a constant resistivity, known as the *residual resistivity* ρ_0. Thus, for nonsuperconducting metals, our definition of the RRR remains appropriate, as the resistivity is expected to remain stable as the temperature approaches 0 K because the number of defects and impurities in the sample is constant. At higher temperatures (150 K - 300 K), however, resistivity exhibits a linear increase which can be attributed to phonon-electron interactions [43]. At 300 K, the measured resistivity is $\rho_{xx} = 6.06 \times 10^{-7}\,\Omega$m, whereas the literature reports a value of $\rho_{xx}(300) = 3 \times 10^{-6}\,\Omega$m [44]. This indicates that the conductivity of the measured crystal surpasses that reported in Ref. [44] by nearly an

order of magnitude. The residual resistivity is $\rho_{xx}(5) = 6.38 \times 10^{-8}\,\Omega$m, yielding a residual resistivity ratio of 9.5. Compared to typical values in alloys, which are approximately ≈ 1, this result is remarkable and underscores the superior properties of our crystal.

Figure 4.5 illustrates the magnetic field dependence of the ordinary magnetoresistance. Measurements were conducted over a broad temperature range, spanning from cryogenic temperatures as low as 2 K to temperatures exceeding room temperature, up to 350 K. To ensure the absence of hysteresis effects, the measurements were performed by sweeping the magnetic field from 13 T to -13 T and back.

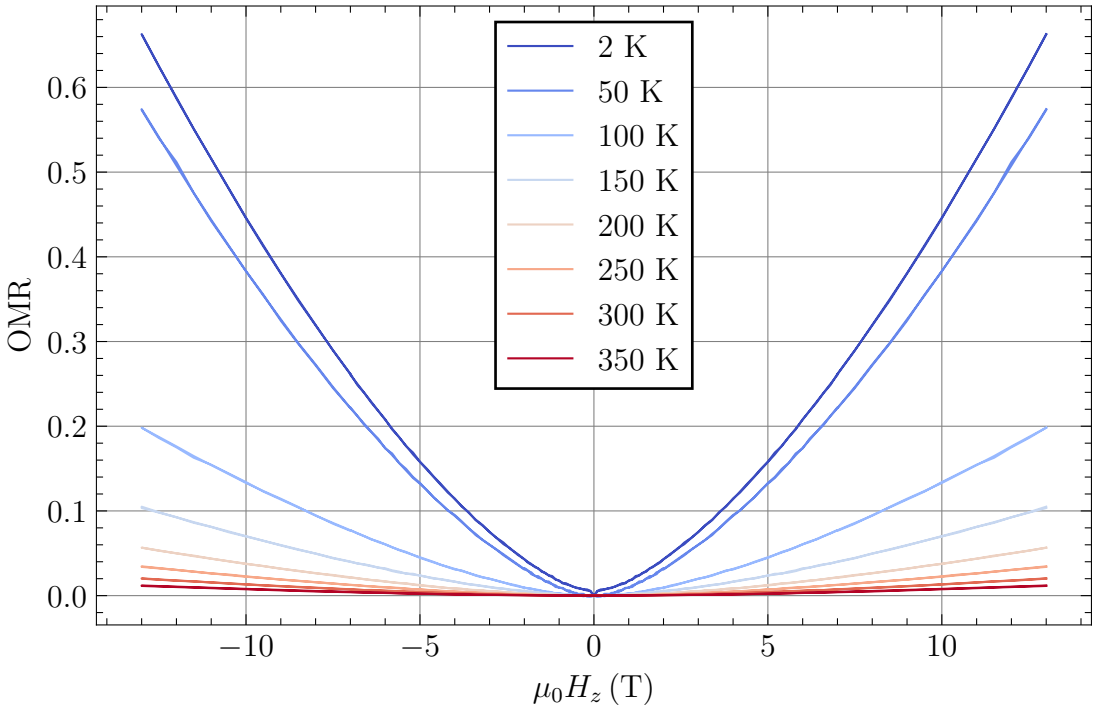

Figure 4.5: Ordinary magnetoresistance at various temperatures.

At all temperatures, the OMR curves show no dependence on the sweep direction, as they overlap perfectly without any visible hysteresis. The quadratic behavior of the longitudinal resistance is clearly observable at low temperatures, such as 2 K, 50 K, and 150 K. At higher temperatures, this behavior may not be immediately apparent; however, upon closer inspection, the quadratic trend can still be noticed. Although the slopes of the ordinary magnetoresistance curves are similar, their values at the maximum field ($\pm$13 T) differ significantly. It is evident that the OMR increases as the temperature decreases. The highest OMR is observed at 2 K, reaching 66.2 %, while the lowest measured OMR occurs at 350 K, with a value of 1.2 %. Additionally, at lower temperatures, the OMR exhibits more pronounced changes within specific temperature intervals, whereas at higher temperatures, the variations become much less significant. Figure 4.6 shows the transverse resistivity as a function of the external magnetic field, measured during sweeps from 13 T to -13 T and back.

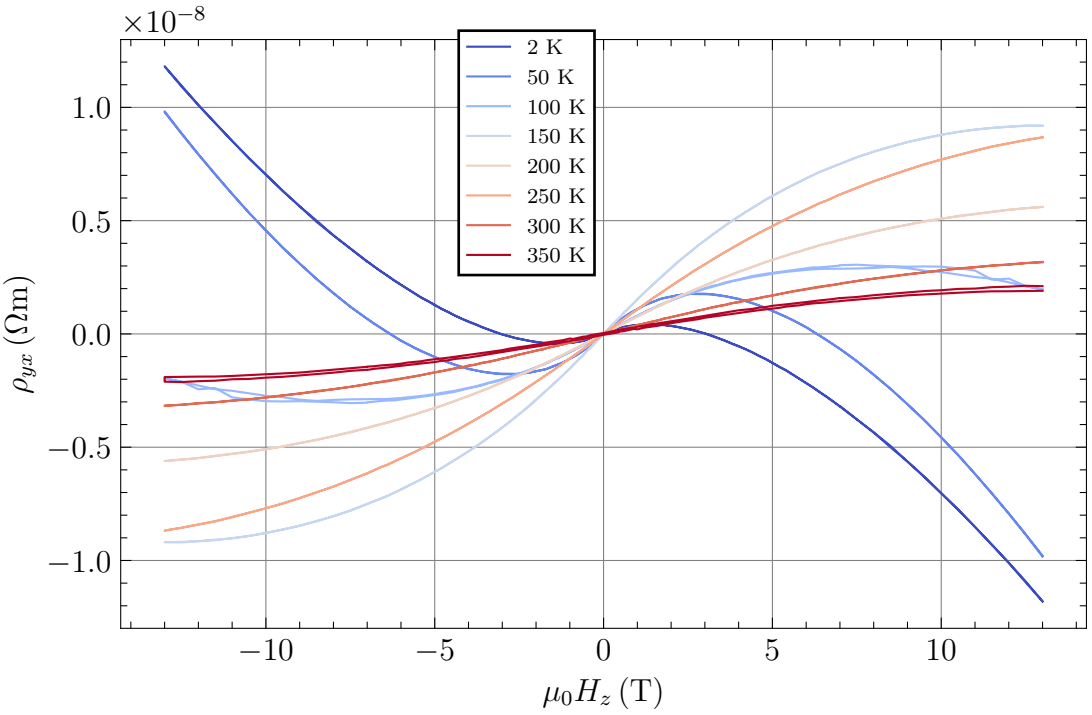

Figure 4.6: Magnetic field dependence of the Hall resistivity at various temperatures. It is worth noting that measurements were also performed at 10 K; however, no significant difference in resistivity was observed compared to the data at 2 K. For the sake of clarity and brevity, the data for 10 K are not included in Figure 4.5 and this one.

The Hall resistivity is about an order of magnitude smaller than the longitudinal resistivity at maximum field across all temperatures and is zero at zero field. Unlike the linear dependence predicted by equation (27), the slopes show an S-shaped signal with a slope change near ±1.3 T at 2 K, which shifts to higher fields with increasing temperature. A second maximum appears near ±2.8 T at 50 K and ±7.5 T at 100 K. Based on these data, we infer that the slope change occurs at approximately ±13 T at 150 K, and it is expected that the slope-changing field will continue to increase at higher temperatures. From measurements of a p-doped GaAs reference sample, it is established that a negative slope in this configuration corresponds to hole-like transport, whereas a positive slope indicates electron-like transport. This observation aligns with equation (27). Based on this, we observe that for low temperatures (2 K, 50 K, and 100 K) within the measured field range, the dominant transport type changes. At low fields ($|\mu_0 H| < 1.3\,\mathrm{T}$ for 2 K), electron contributions dominate. In contrast, at higher fields ($|\mu_0 H| > 1.3\,\mathrm{T}$), transport is predominantly hole-like. For higher temperatures, only a positive slope is observed throughout the field range of ±13 T, indicating electron-like transport remains dominant at all measured fields.

The Hall resistivity slopes resemble anomalous Hall effect (AHE) measurements observed in altermagnetic MnTe, which also crystallizes in the NiAs structure [45]. However, a spontaneous AHE contribution is forbidden in CrSb when the c-axis is out of plane due to symmetry constraints, as discussed in Refs. [45, 46]. The AHE could still arise from canting of the compensated magnetic order if the spin-flop field is exceeded. SQUID measurements

show no deviations from linearity, indicating no change in magnetic ordering within the measured field range. Ab initio calculations further suggest the spin-flop field is about 25 times higher than the maximum applied field, excluding AHE detection. The temperature dependence and absence of hysteresis also indicate the S-shape of the Hall data is not due to the AHE. Instead, an alternative, nonmagnetic explanation seems more plausible for this behavior, which is consistent with existing literature [46]. A closer examination of the slope of the Hall resistivity at 2 K reveals that the curve follows the form:

$$\rho_{yx}(B) = \frac{aB - bB^3}{c + dB^2} \tag{38}$$

with prefactors a, b, c and d. This functional form closely resembles equation (29) from the two-band model, which is given as:

$$\rho_{yx}(B) = \frac{1}{e} \frac{(n_e\mu_e^2 - n_h\mu_h^2)B + (n_e - n_h)\mu_e^2\mu_h^2 B^3}{(n_e\mu_e + n_h\mu_h)^2 + (n_e - n_h)^2\mu_e^2\mu_h^2 B^2}. \tag{39}$$

The sign of the dominant B^3 term implies $n_e < n_h$. This observation supports the negative, hole-like slope of the Hall resistivity. Given the resemblance of equation (39) to the observed behavior, it is reasonable to use this equation to determine the carrier densities and mobilities of the two carrier types. In Figure 4.7, the measured data at 2 K are shown alongside four different fits. These include not only a one- and two-carrier fit but also three- and four-carrier fits, using equation (26) to extract the parameters n_i and μ_i.

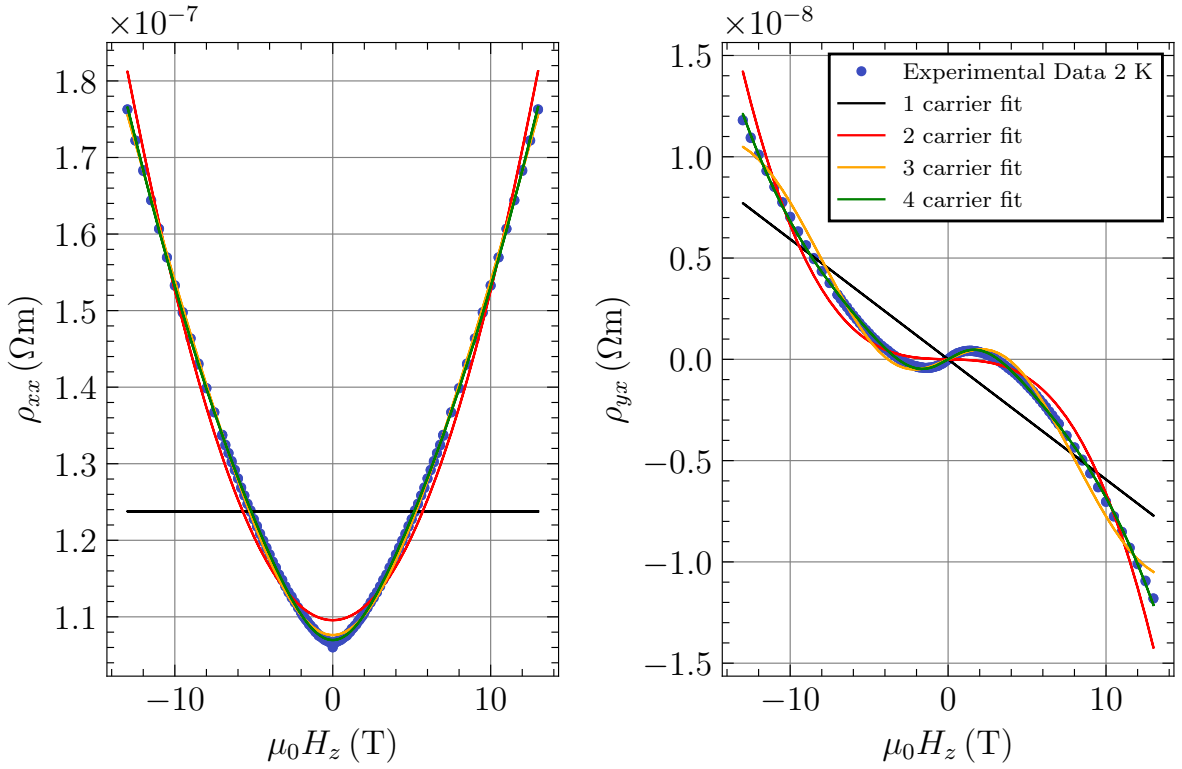

Figure 4.7: Longitudinal and Hall resistivity ρ_{yx} at 2 K, along with the results of multi-carrier fitting for one, two, three and four carriers.

It is clearly evident that the deviations of the fits from the experimental data decrease as the number of carriers — and consequently the number of parameters — increases. As previously described, the ordinary magnetoresistance remains constant in the one-band model. Consequently, the one-carrier fit results in a flat line. The fit of the Hall resistivity does not exhibit any slope change as expected; however, the overall slope aligns reasonably well with the experimental data. For the longitudinal resistivity, the two-carrier fit shows slight discrepancies across all field values, while the three-carrier fit only deviates in the low-field range. The four-carrier fit, however, matches the data perfectly at almost all fields. For the Hall resistivity, every fit exhibits some level of deviation, particularly in the low-field range. Further the two-carrier fit does not reveal the characteristic slope-change from negative to positive at $|\mu_0 H| < 1.3\,\mathrm{T}$, as shown in greater detail in Figure 4.8.

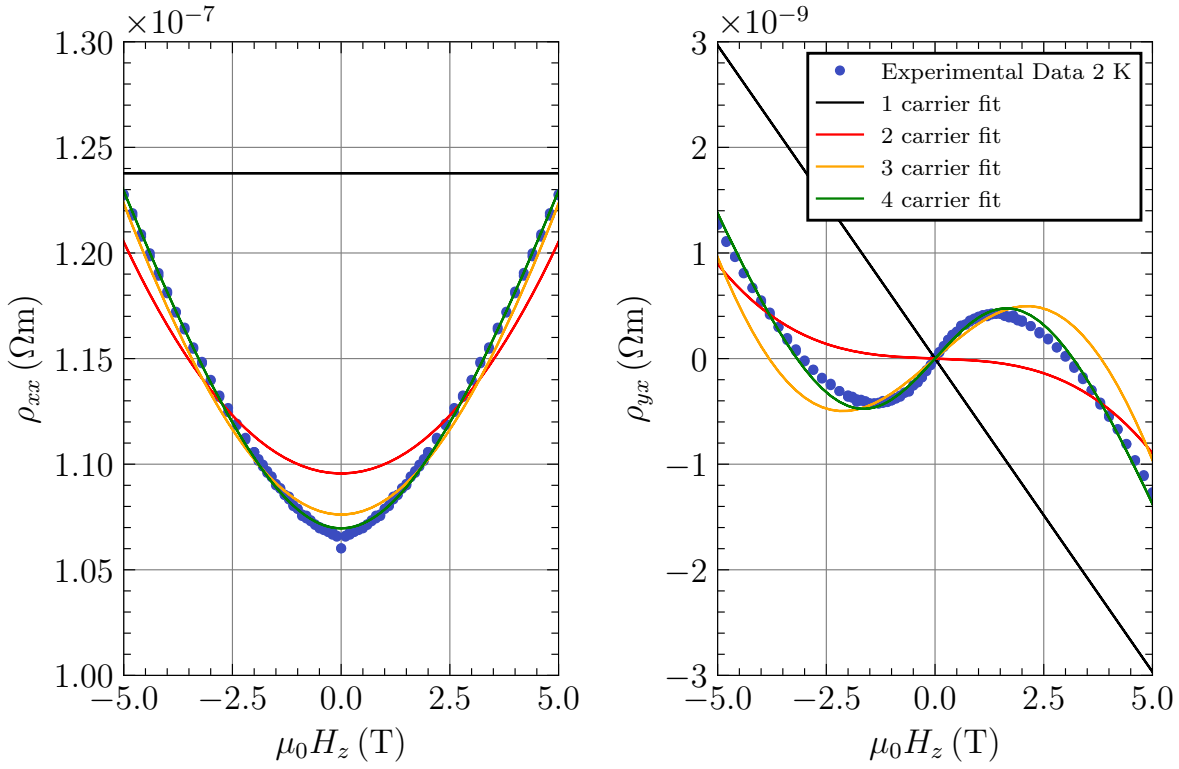

Figure 4.8: Detailed view of the data and fits shown in Figure 4.7.

Additional fits incorporating five and six types of carriers were performed, resulting in progressively improved fit quality. In the case of the six-band fit, the agreement between the fit and the measured data is nearly perfect, with minimal deviations observed across the entire field range. Taking the derivative of the two-carrier fit for the transverse resistivity reveals that the slope stays negative throughout the entire field range. Consequently, the distinctive S-shape characteristic of the Hall resistivity is not captured in this initial application of the two-band model. In the following table, the densities and mobilities from the fitting are shown.

Carrier Densities n_i (cm^{-3})						
	n_e	n_h	n_{e2}	n_{h2}	n_{e3}	n_{h3}
1 carrier	–	1.05×10^{22}	–	–	–	–
2 carrier	$\mathbf{3.52 \times 10^{20}}$	$\mathbf{5.65 \times 10^{20}}$	–	–	–	–
3 carrier	1.07×10^{21}	3.35×10^{20}	9.65×10^{19}	–	–	–
4 carrier	$\mathbf{3.69 \times 10^{20}}$	$\mathbf{5.91 \times 10^{20}}$	1.95×10^{19}	4.36×10^{19}	–	–
5 carrier	8.16×10^{20}	4.12×10^{20}	4.9×10^{18}	7.6×10^{18}	1.63×10^{20}	–
6 carrier	$\mathbf{3.75 \times 10^{20}}$	$\mathbf{5.23 \times 10^{20}}$	5.52×10^{19}	1.14×10^{20}	2.01×10^{18}	1.45×10^{18}
Carrier Mobilities μ_i (cm^2/Vs)						
	μ_e	μ_h	μ_{e2}	μ_{h2}	μ_{e3}	μ_{h3}
1 carrier	–	48	–	–	–	–
2 carrier	**713**	**564**	–	–	–	–
3 carrier	192	743	1308	–	–	–
4 carrier	**578**	**445**	2339	1419	–	–
5 carrier	172	622	3932	2496	920	–
6 carrier	**475**	**390**	1368	969	5439	4527

Table 1: Carrier densities n_i and mobilities μ_i of bulk CrSb deduced from one-, two-, three-, four-, five-, and six-carrier fitting. The upper section presents carrier densities, and the lower section shows mobilities.

In the one-band model, the density of the hole-like carrier band is significantly higher than in any other model, exceeding the densities in the two-band model by more than one order of magnitude. Additionally, the mobility, μ_h, in this model is so low that it strongly suggests an inadequate description of the measured data. Assuming electron-like transport in the one-band model yields unphysical parameters, consistent with the observation that the overall slope of the curve should be positive for electron-dominated transport. Similar issues arise in the three-carrier fit if a second hole-like carrier is introduced, leading to unphysical values such as $n_{h2} > 10^{24}$ cm^{-3} or $\mu_{h2} < 0.1$ cm^2/Vs, and the situation worsens when adding a third hole-like band in the five-carrier fit. Notably, these fits also show poorer agreement in the low-field regime. The three-band model introduces a third band with significantly lower density than the others but very high mobilities, a trend that persists in the four-, five-, and six-band models. However, in the five- and six-band fits, n_{e3} reaches densities substantially higher than n_{e2} and n_{h2}, while the mobilities μ_{e2} and μ_{h2} — already extraordinarily high in the four-band model — become unrealistically high for μ_{e3} and μ_{h3}. In general, the one-, three-, and five-carrier parameters show considerable deviation from corresponding carrier types in other models. Conversely, the results for n_e and n_h in the two-, four-, and six-band fits remain relatively consistent (marked in bold), with a slight decrease in the mobilities, but still within a reasonable range. However, discrepancies in n_{e2} and n_{h2} indicate that these parameters no longer align across the models.

The values for densities and mobilities obtained from the four-carrier fit align closely with those reported in Ref. [46], where the authors observed similar trends as depicted in Figures 4.5 and 4.6. A key argument made in Ref. [46] supporting the presence of multiple carrier types is the improved agreement of the fit when moving from a two-carrier to a four-carrier model. They propose the existence of two electron- and two hole-type carriers, with one of each characterized by low density and simultaneously high mobility.

While the improved fit with an increased number of parameters is unsurprising, the absence of a slope change in the two-carrier fit does not necessarily preclude the validity of the two-band model. The constancy of the carrier densities n_e and n_h in the two-, four-, and six-band models further strengthens the suspicion that the transport behavior can be well described by a two-carrier type model. This suggests that excluding this possibility may not be justified. Figure 4.9 displays the results of a mobility spectrum analysis for the data at 2 K.

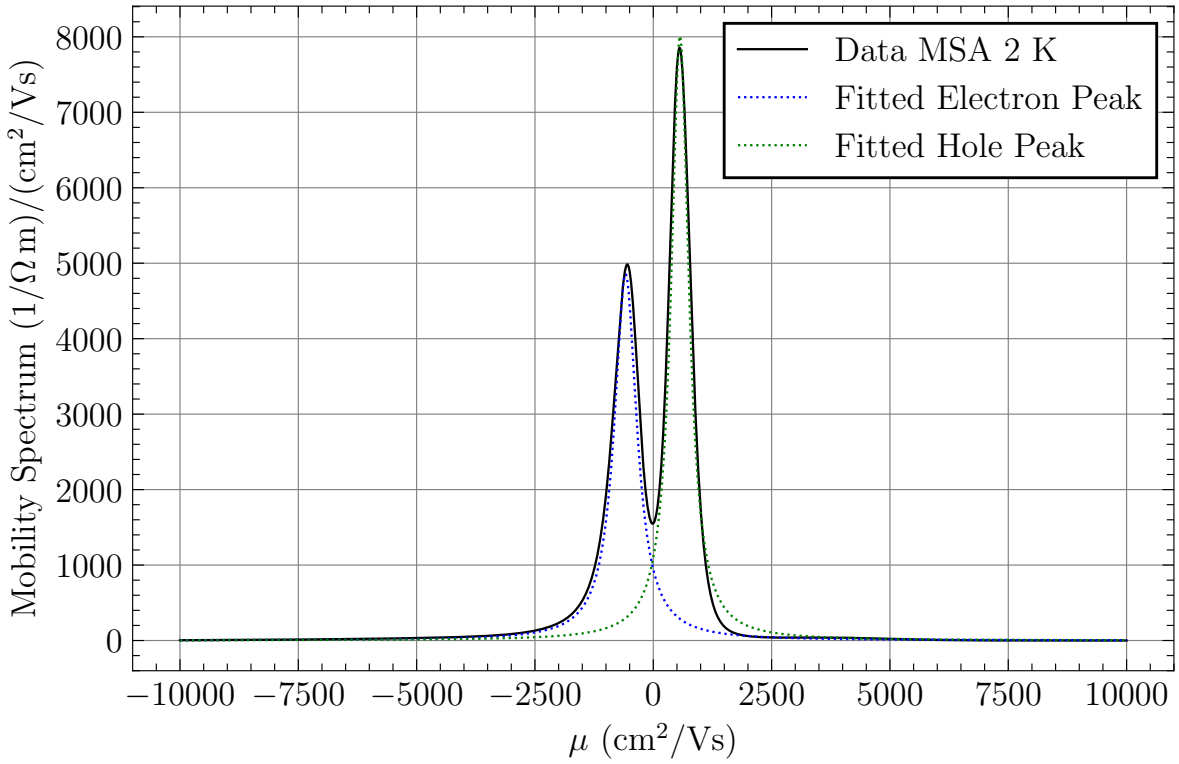

Figure 4.9: Mobility spectrum from the longitudinal an transversal resistivity of CrSb single crystals at 2 K. The calculations were performed by Michał Baj.

The presence of two peaks strongly indicates a two-carrier transport behavior. Notably, in the convention of MSA, the mobilities of electrons and holes have opposite signs. The MSA result clearly does not exhibit two delta distributions as one would expect in a discrete spectrum, but instead shows two peaks, which can be fitted with overlapping Lorentz functions. The peak positions, corresponding to the maximum mobilities, are determined to be $\mu_e = 586$ cm^2/Vs and $\mu_h = 564$ cm^2/Vs. While the electron mobility deviates by 18 % from the two-band fit, the hole mobility remains remarkably consistent between both approaches. This consistency suggests that the mobilities obtained from the MSA align well with the previously presented fits. By integrating the Lorentzians and dividing by the elementary charge, the carrier densities are found to be $n_e = 2.69 \times 10^{19}$ cm^{-3} and $n_h = 3.49 \times 10^{19}$ cm^{-3}. This approach yields densities an order of magnitude lower than those obtained from the two-band model. Ref. [39] highlights that measuring Hall data at seven or more fields can yield unphysical results. In such cases, the mobility spectrum analysis provides approximate solutions, with the closest being a set of discrete carrier mobilities.

4.3 Magnetotransport in Thin Films

A challenge in bulk measurements is that the current direction is not well defined. Due to the large sample volume and the imprecise positioning of the contacts, it is unlikely that the charge carrier velocity can be strictly defined as $\vec{v} = (v_x, 0, 0)$. This issue can be resolved using a lithographically defined *Hall-bar* of a thin film. In the photolithography process, a photomask is applied along with a photoresist in the desired shape. The resist in unwanted areas is exposed and subsequently developed, leaving only the desired pattern. Finally, the unwanted regions of the sample are etched away. Figure 4.10 shows a lithographically fabricated Hall-bar.

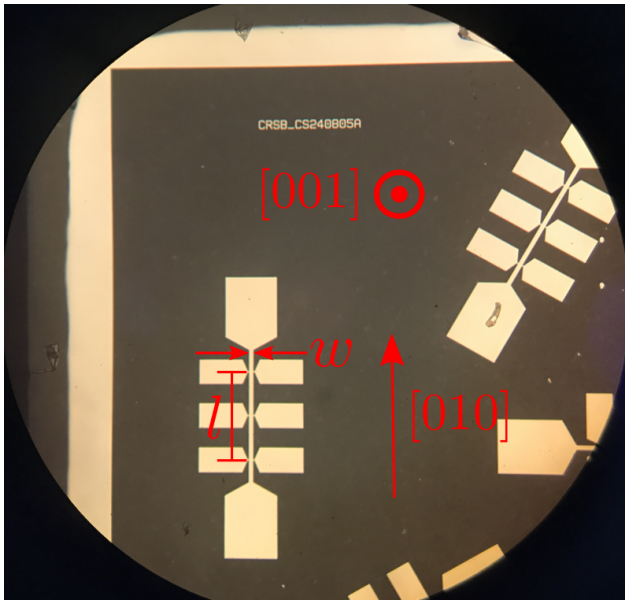

Figure 4.10: Hall-bars on the thin film sample *CS240805A*. Bright regions correspond to the CrSb/PtSb multilayer film after the lithography process, while dark regions indicate the SrF_2 substrate. A negative photoresist was used, and etching was performed via argon milling.

As previously mentioned, the thicknesses of the individual layers are 15 nm for PtSb and 25 nm for CrSb. The surface of the film is parallel to the (001) plane, equal to the bulk geometry. The current channel has a length of $l = 1$ mm and a width of $w = 50$ µm. This indicates that for the longitudinal resistance measurement, the current path consists of 20 squares. Additionally, the thin film samples were also contacted using gold wires and small pieces of indium. Based on the XRD measurements, specifically the pole figure shown in Figure 2.11, the current direction corresponds to the [010] crystallographic direction of CrSb. The applied current in all thin film measurements was 10 µA which refers to a current density in the multilayer of $j = 5 \times 10^6$ A/m^2.

Due to the fact that we have a multilayer film, some considerations need to be made when it comes to the resistivity separation of the two compounds. In order to extract the magnetotransport data of pure CrSb, a second sample was measured which contains only a 15 nm PtSb layer, so that it has the same thickness as the PtSb in the multilayer sample. Considering the two samples in terms of conductivity offers a practical framework, as demonstrated by the following equations. In case of the longitudinal conductivity, we consider the system of the multilayer as a parallel circuit, where we can assume

$$\sigma_{xx}^{\mathrm{I+II}} = \sigma_{xx}^{\mathrm{I}} + \sigma_{xx}^{\mathrm{II}} \tag{40}$$

where $\sigma_{xx}^{\mathrm{I+II}}$ is the longitudinal conductivity of the multilayer sample, while σ_{xx}^{I} and $\sigma_{xx}^{\mathrm{II}}$ correspond to the longitudinal conductivities of the PtSb and CrSb layers, respectively. That approach yields the same result as the two-band model. For the transverse conductivity $\sigma_{yx}^{\mathrm{I+II}}$, this equation is not applicable. Instead, the system must be characterized by the ratio of transverse conductivity to overall conductivity, leading to the introduction of the Hall angle:

$$\alpha = \frac{\sigma_{yx}}{\sigma_{xx}} \tag{41}$$

It is important to note that, in this framework, all quantities must be expressed in sheet units. This requires converting resistivity into conductivity by accounting for the thickness t of the films. Specifically, the sheet resistance is defined as:

$$R_{\square} = R\frac{w}{l}. \tag{42}$$

For the transverse configuration, w is equal to l, meaning the measured resistance directly corresponds to the sheet resistance. To obtain the transverse conductivity of the CrSb layer, we model the two layers as two parallel resistors. The current flowing through each layer depends on the longitudinal resistances of the individual layers, with the greater part of the current flowing through the layer with lower resistance. This impacts the Hall effect, as it is proportional to the applied current density. Since part of the total current flows through the PtSb layer, the Hall contribution from the CrSb layer is influenced. Additionally, when charge carriers accumulate on one side of the sample in one layer, they can be discharged by the other layer. Therefore, the bilayer sample can be considered as a closed circuit of two resistors connected in series. Taking this into account, the Hall resistance of the bilayer sample is given by:

$$R_{yx}^{\mathrm{I+II}} = R_{xx\square}^{\mathrm{I+II}}\left(\frac{\sigma_{xx\square}^{\mathrm{I}}\alpha^{\mathrm{I}} + \sigma_{xx\square}^{\mathrm{II}}\alpha^{\mathrm{II}}}{\sigma_{xx\square}^{\mathrm{I}} + \sigma_{xx\square}^{\mathrm{II}}}\right). \tag{43}$$

Note that the ratio of the thicknesses of the two layers plays a significant role in this equation. To determine the contribution of the total Hall resistivity of CrSb in the multilayer system, equation (43) must be solved for α^{II}. This result is then converted into resistivity by multiplying by the thickness of the CrSb layer. Remarkably, to apply equation (40) and equation (43), all measured resistances must correspond to the same applied magnetic field. Due to slight inaccuracies in the field measurements in the PPMS, the data were interpolated within the measured field range of ± 13 T. It is also important to note that this model is highly simplified and does not account for interface phenomena or other complex effects. All subsequent measurements were conducted using the same samples: *CS240805A*, described in Section 2.2, and the PtSb 15 nm sample *PS240731A*.

Figure 4.11 shows the temperature dependence of the longitudinal resistance and resistivity of the PtSb/CrSb film, the buffer layer PtSb and the CrSb layer extracted with equation (40). The slopes of all three curves indicate a metallic behavior. Between approximately 20 K and 300 K, a clear linear increase in resistance and resistivity is observed for both layers. Additionally, the residual resistivity ratios of all systems exhibit similar values. Reducing

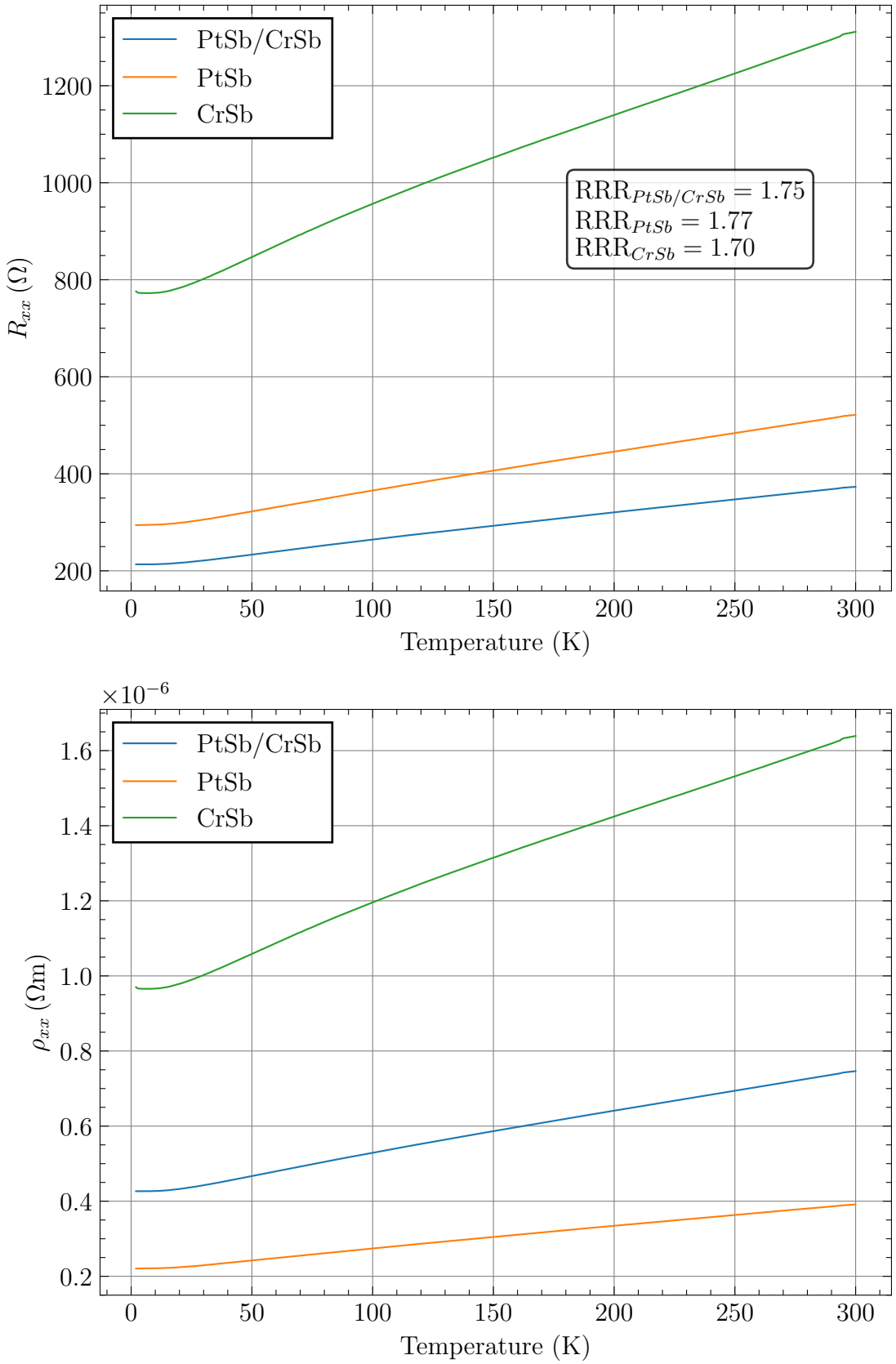

Figure 4.11: **Top:** Longitudinal resistance R_{xx} vs. temperature. **Bottom:** Longitudinal resistivity ρ_{xx} vs. temperature.

the thickness of a thin film, surface scattering can emerge as the primary scattering mechanism [47]. Therefore, it is expected that the resistance of the multilayer film is the lowest, as it is the thickest. As the thickness increases, the material becomes more bulk-like, and surface interactions become less significant [47]. Additionally, the decreasing size of grain boundaries in polycrystalline films may contribute to higher resistance at smaller thicknesses [47]. Since the films in this study are epitaxially grown, as detailed in Section 2.2, this contribution can be disregarded. The significantly higher resistivity of CrSb compared to PtSb can likely be attributed to the intrinsic differences between the two compounds. Additionally, a smaller contribution to this difference may arise from oxidation-related resistance, as the measured films are uncapped. Another minor factor could be the varying density of point defects in these layers, resulting in different scattering mechanisms for charge carriers. Considering the resistivity, the arrangement of the three curves changes. While the CrSb layer still exhibits the highest resistivity, the multilayer sample now has a higher resistivity than the PtSb sample. This reordering between PtSb and the PtSb/CrSb bilayer is not unexpected when taking into account the ratios of their resistances and thicknesses. The resistance of the PtSb sample is greater than that of the multilayer sample, while its thickness is smaller. Consequently, the resistivity of the PtSb sample is lower. In Figure 4.12, the magnetic field dependence of the longitudinal resistance is presented for all three systems at 5 K.

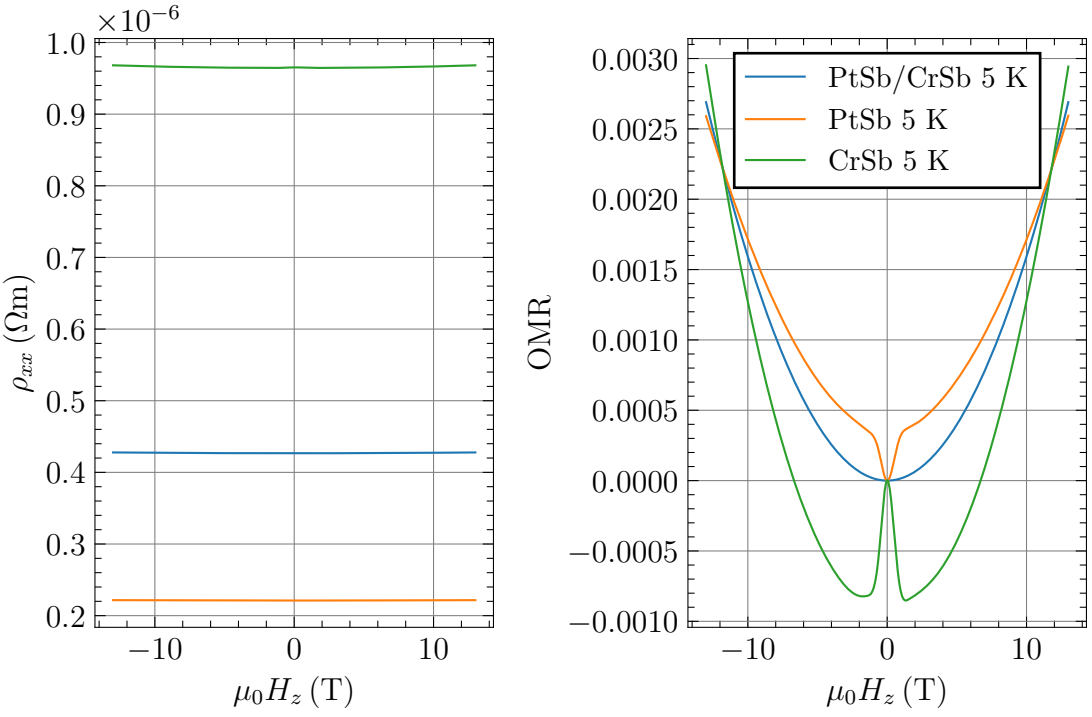

Figure 4.12: **Left:** Longitudinal resistivity ρ_{xx} vs. external field. **Right:** Ordinary magnetoresistance. The measurements were performed at 5 K.

Examining the raw longitudinal resistance data on the left side reveals values consistent with the temperature sweep measurements at zero field. Furthermore, ρ_{xx} appears to remain unchanged under the applied magnetic field for both individual layers and the multilayer sample. Upon transforming the data using equation (23) to calculate the ordinary magnetoresistance, a nonconstant slope becomes evident in all three curves. For the PtSb/CrSb

multilayer sample, the signal exhibits a quadratic dependence on the magnetic field, reaching a maximum magnetoresistance of 0.27 % at ±13 T. In the case of PtSb, while the slope is also quadratic at higher fields, there is an almost linear dip toward zero within the range $|\mu_0 H| < 1$ T. This behavior is likely attributable to the phenomenon of *weak localization*, a quantum mechanical effect characterized by the formation of stationary electron wavefunctions in disordered systems [48]. Interestingly, this weak localization effect vanishes when a CrSb layer is introduced atop the PtSb layer. It is noteworthy that the observed resistivity of CrSb in Figure 4.12 is not directly measured but rather inferred from the two measured samples. Consequently, the inverse dip in CrSb, and thus the observed negative magnetoresistance, is not physical. Given that the bilayer sample exhibits a quadratic field dependence, it is reasonable to infer that CrSb alone follows a similar trend. Hence, the apparent dip can be disregarded, and the curve can be shifted to reflect zero magnetoresistance at zero field. The previously observed deviation from the quadratic slope at low magnetic fields was also evident in the measurements conducted at 10 K. Consequently, the curves for 5 K and 10 K in Figure 4.13 were adjusted to align at zero field, facilitating the extraction of magnetoresistance at maximum field. It is notable that the effect observed in PtSb is less pronounced at 10 K compared to 5 K.

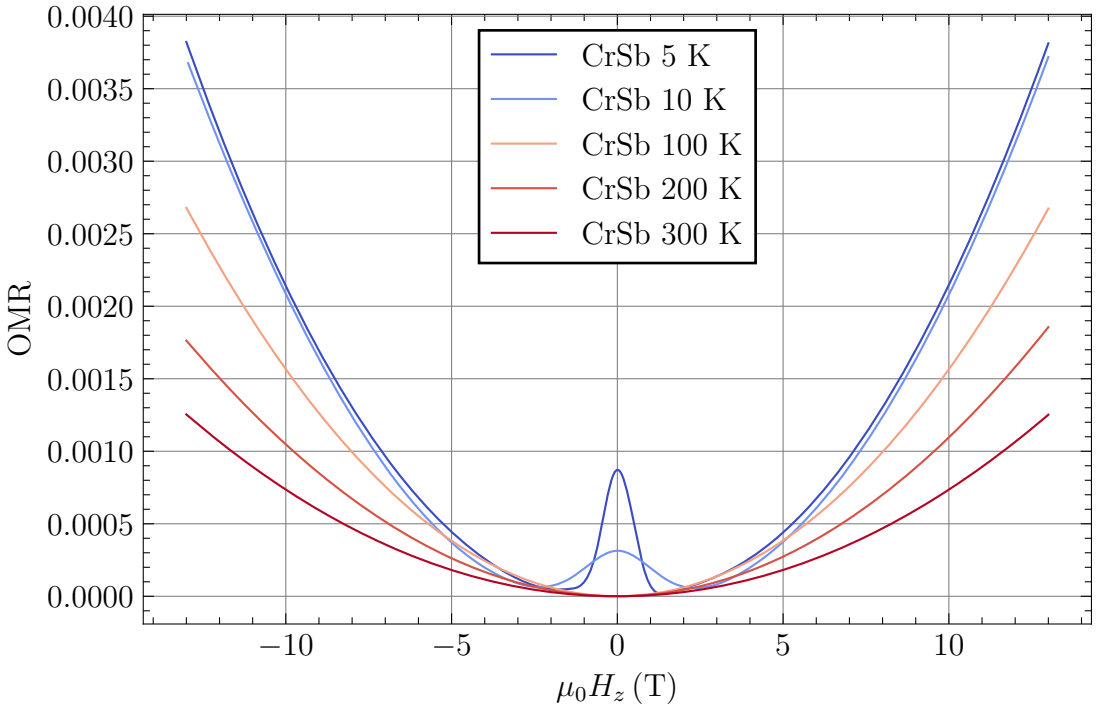

Figure 4.13: Ordinary magnetoresistance at various temperatures.

As anticipated, the OMR diminishes with increasing temperature, which can be attributed to the dominance of thermal phonon scattering. Figure 4.14 shows the transverse resistance of all three systems at 5 K. In this configuration, the resistance corresponds to the sheet resistance, representing the resistance per unit square. It is immediately apparent that the transport behavior of the CrSb layer differs from that of the PtSb layer, resulting in a combined effect in the multilayer sample. As mentioned in the explanation of equation (43), the short-circuiting of accumulated charge carriers plays a role. Measurements of a reference sample indicate that the positive slope of the PtSb Hall resistance corresponds

to electron-dominated transport. In contrast, the extracted CrSb layer exhibits a negative slope in its resistance—similar to bulk CrSb—indicating hole-dominated transport in this layer. This means that in the bilayer, charge carriers of different types in the two layers are deflected to opposite edges of the sample. An intuitive explanation for the intermediate slope of the bilayer is that the accumulated carriers in one layer are partially neutralized by those in the other, leading to a cancellation effect.

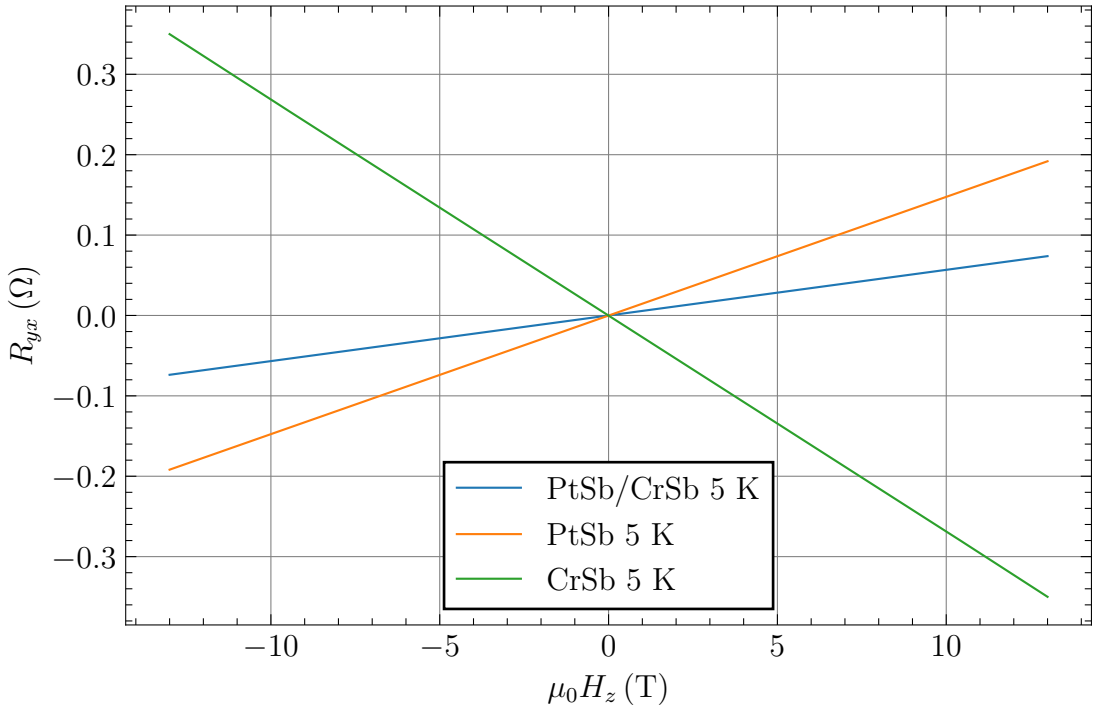

Figure 4.14: Transversal sheet resistance R_{yx} vs. external field at 5 K.

The strictly linear behavior indicates a single-band, single-carrier transport mechanism. The results from fitting the data using the one-, two-, and three-band models are presented in the following table.

	Carrier Densities n_i (cm^{-3})		
	n_e	n_h	n_{h2}
1 carrier	–	9.29×10^{21}	–
2 carrier	5.86×10^{20}	7.88×10^{20}	–
3 carrier	5.82×10^{20}	4.16×10^{20}	3.75×10^{20}
	Carrier Mobilities μ_i ($\mathrm{cm}^2/\mathrm{Vs}$)		
	μ_e	μ_h	μ_{h2}
1 carrier	–	6.96	–
2 carrier	47.1	47.13	–
3 carrier	47.26	47.01	47.01

Table 2: Carrier densities n_i and mobilities μ_i of the CrSb layer deduced from one-, two- and three-carrier fitting. The upper section presents carrier densities, and the lower section shows mobilities.

The values obtained from the hole-like single-carrier model of the CrSb layer suggest a band with a high carrier density but low mobility. Performing the fit under the assumption that electrons are the charge carriers fails entirely, reinforcing the conclusion that holes dominate the transport in the film. The parameters derived from the two-carrier model suggest a trend towards two bands with lower carrier densities but slightly higher mobilities. At first glance, the results from the three-carrier fit might appear plausible, but the parameters exhibit standard deviations of up to approximately $\pm 10^8$ %. Furthermore, the results are highly sensitive to the initial fitting parameters, indicating poor fit stability. This leads to the conclusion that the one-carrier model appropriately describes the transport behavior in the film. After accounting for the layer thicknesses by multiplying the resistance with the respective thicknesses, the resistivity of the multilayer and the PtSb sample becomes nearly identical. In contrast, the slope of the CrSb resistivity becomes less steep compared to that of the multilayer sample. In Figure 4.15, the Hall resistivity of CrSb at various temperatures is shown. All curves exhibit a linear slope. At 200 K, a small kink appears around 10 T, which can be attributed to the lower data density in this measurement; the interpolation of the data likely created this artifact. A slight trend in the slopes is visible: while the gradient is largest at the lower temperatures, it decreases with increasing temperature. Notably, 200 K exhibits a lower gradient than 300 K.

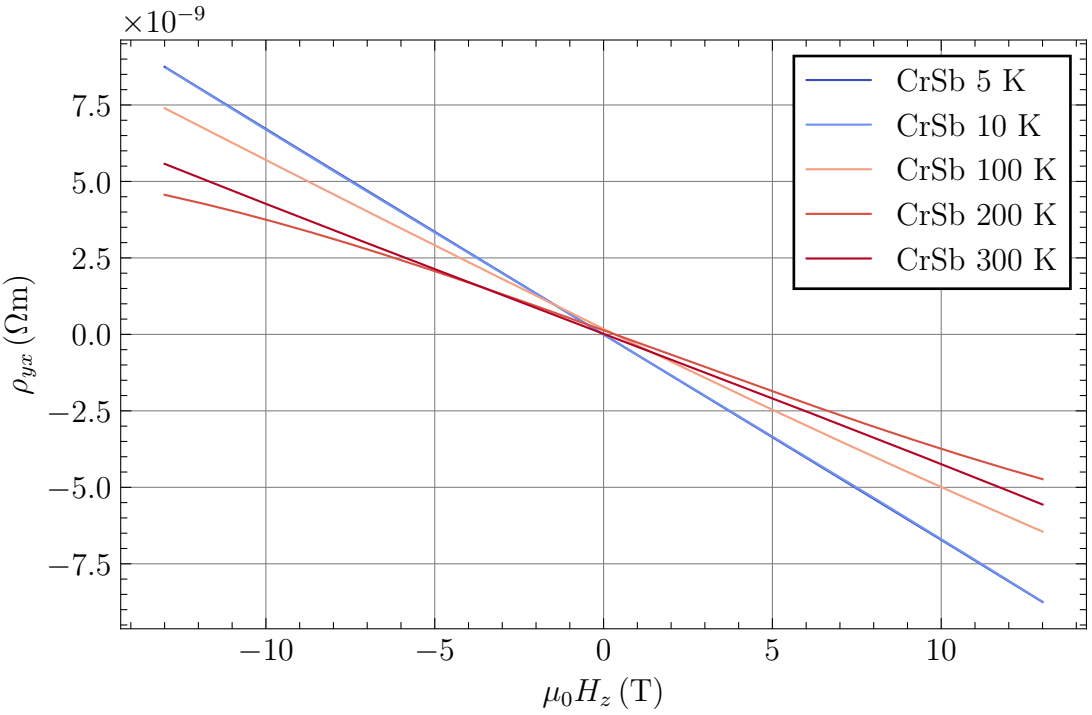

Figure 4.15: Magnetic field dependence of the Hall resistivity at various temperatures.

4.4 High-Field Experiments

Although the ab initio calculations predict the spin-flop field to exceed the highest magnetic field ever generated, making its occurrence in the PPMS unlikely, pursuing its observation is still worthwhile. This is because theoretical predictions can sometimes fail, and such experiments allow us to approach the predicted threshold while also examining whether the resistivity behavior observed in low fields extends into higher fields. Consequently, measurements were performed in pulsed field experiments at the high-field laboratory of Helmholtz Zentrum Dresden-Rossendorf (HZDR). In this facility, high magnetic fields are generated for short durations through the rapid discharge of large capacitors, which drive large currents through coils. The coil selected for this experiment was capable of reaching a maximum field of ±68.68 T. The duration of each pulse was on the order of 100 ms, during which resistance was measured using alternating current (AC) over the entire pulse time. This process includes an upsweep from zero field to the maximum field, followed by a downsweep. A second pulse with the opposite field direction was then applied. Such experiments are highly susceptible to noise. The sample used was fabricated from a bulk crystal, which was sourced from the same batch as the crystal used in Section 4.2. To minimize noise and ensure a defined current direction, the sample was processed into a microstructure via focused ion beam (FIB) cutting. The dimensions of this microstructure are $l = 32$ µm, $w = 4$ µm and $t = 2$ µm. For the following measurements the applied current of 100 µA was generated in the [110] direction of CrSb. Figure 4.16 displays the longitudinal resistivity measurements at 4.2 K and 300 K, with the magnetic field aligned parallel to the c-axis of CrSb. A clear quadratic behavior of ρ_{xx} is observed within the whole field range, with lower resistivity at 4.2 K compared to 300 K, as expected. Additionally, the longitudinal resistivity exhibits a more pronounced change with the applied field at 4.2 K than at 300 K.

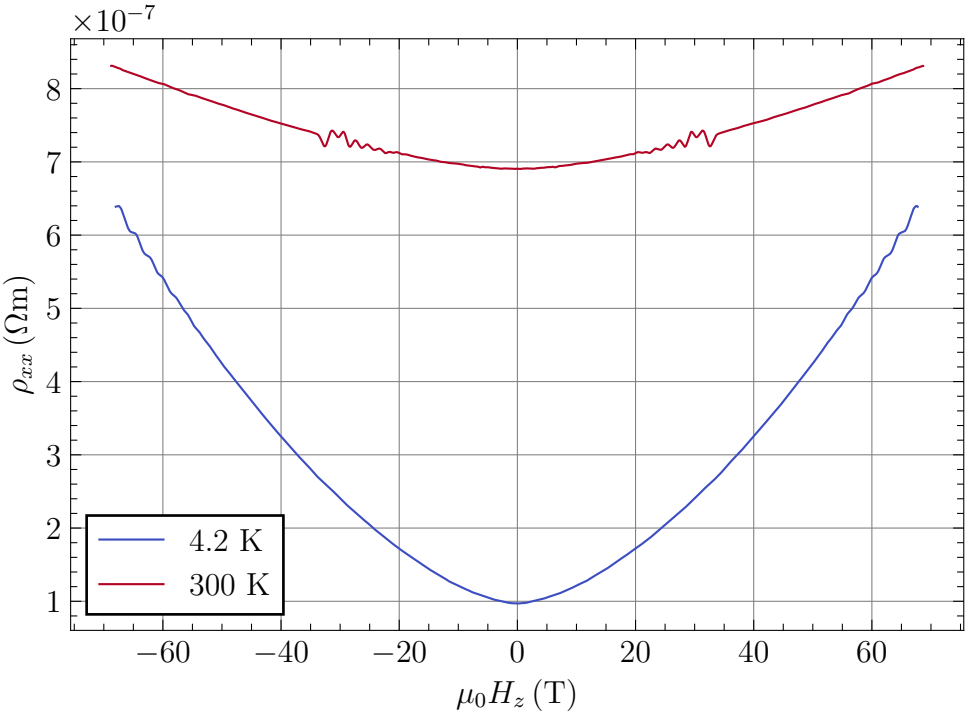

Figure 4.16: Longitudinal resistivity ρ_{xx} obtained from a pulsed field measurement.

The data within the field range of ±13 T align perfectly with the bulk data obtained from the PPMS measurements. The oscillations observed in the 4.2 K data for $|\mu_0 H_z| > 60\,\mathrm{T}$ are attributed to magnetic quantum oscillations, which will not be discussed further in this work. In contrast, the noise present in the 300 K data around $\mu_0 H_z \approx \pm 30\,\mathrm{T}$ originates from the measurement setup. This noise becomes even more significant when examining the Hall resistivity, shown in Figure 4.17. While a characteristic slope change at 300 K, which was almost visible in Figure 4.6, is now more apparent around ±30 T, it remains challenging to pinpoint the exact field at which this change occurs, due to data outliers.

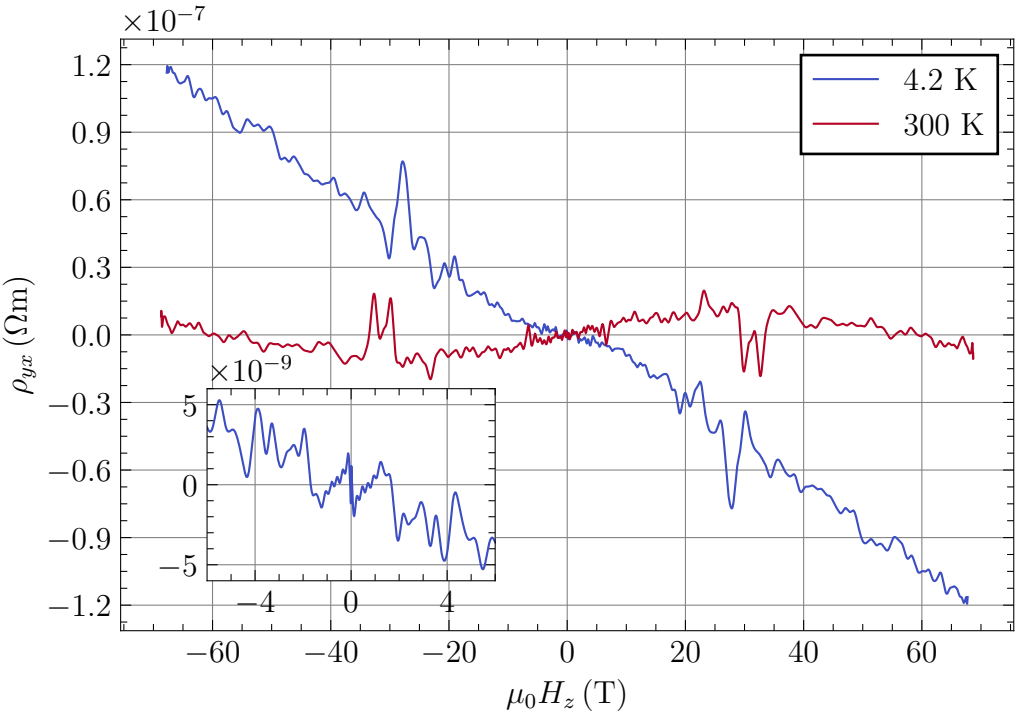

Figure 4.17: Hall resistivity ρ_{yx} obtained from a pulsed field measurement.

Furthermore, the slope change expected at $|\mu_0 H_z| \approx 1.3\,\mathrm{T}$ is entirely obscured by noise, as illustrated in the inset of Figure 4.17. This demonstrates that pulsed field measurements are not well-suited for investigating low-resistivity signals. However, the 4.2 K measurement reveals that no further slope changes occur in the high-field regime ($|\mu_0 H_z| > 13\,\mathrm{T}$). This observation is consistent with the multicarrier fitting results at low temperatures, extended to a field range of ±70 T for both the even-numbered carrier models and the single-band model. However, in the case of the three- and five-band models, the slope of the fit transitions to an overall positive slope at approximately $|\mu_0 H_z| \approx 20\,\mathrm{T}$. This further reinforces the notion that the odd-number carrier models are inadequate for accurately describing the transport behavior in bulk. For the transverse resistivity at 300 K, it appears to follow the same trend observed at all other measured temperatures with the PPMS, showing an overall negative slope at high fields. Additionally, the Hall resistivity of the measured microstructure closely matches the bulk measurements previously obtained using the PPMS. The main result, however, of the high field experiments is that there is still no indication on the spin-flip or spin-flop phenomenon and no anomalous Hall effect up to $|\mu_0 H_z| = 68.68\,\mathrm{T}$.

5 Discussion and Conclusion

When comparing the longitudinal resistance of bulk and thin films, it is notable that the longitudinal resistance in thin films differs from that in bulk material by approximately a factor of 10^7, primarily due to the significant difference in their thicknesses. A more appropriate quantity for comparison is the resistivity, as it is normalized to the sample's volume. Figure 5.1 presents the resistivity of CrSb in both bulk and thin-film forms.

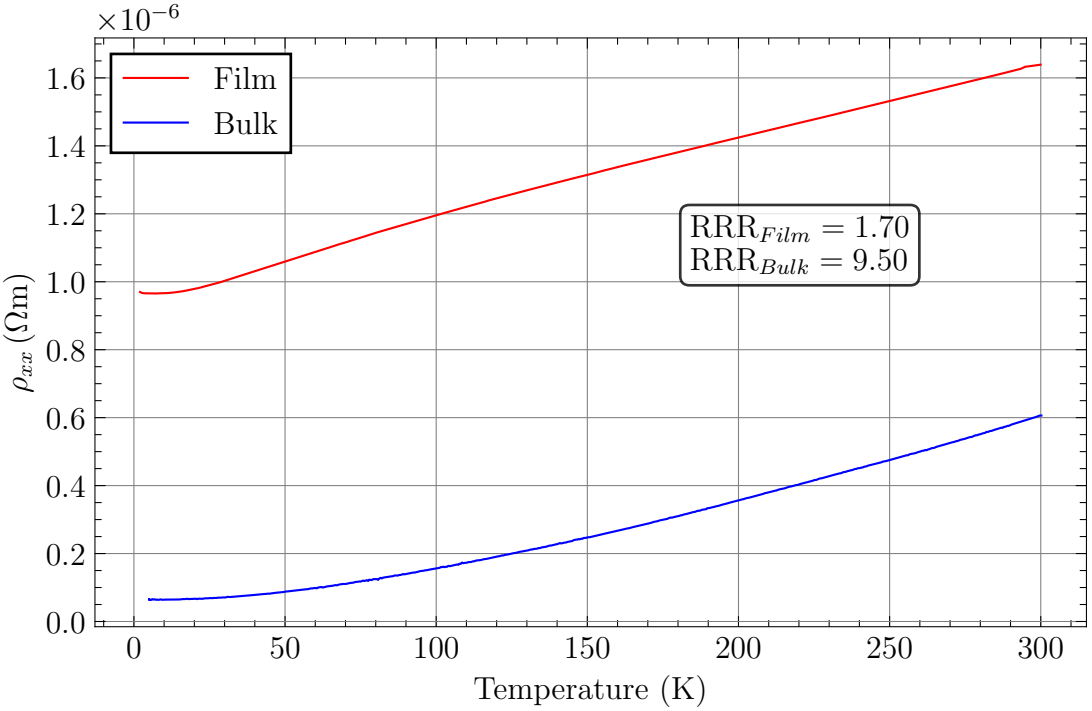

Figure 5.1: Comparison of $\rho_{xx}(T)$ in bulk (blue) and thin film (red).

It is evident that the resistivity of the thin film is significantly higher than that of the bulk material, with the residual resistance differing by approximately a factor of ≈ 16. This discrepancy can be attributed to the fact that in bulk materials, charge carrier scattering is primarily dominated by phonons and impurities, as previously discussed. However, in thin films, additional scattering mechanisms, such as surface scattering [47], must also be considered. The room-temperature resistivity of the thin film is $\rho_{xx}(300) = 1.64 \times 10^{-6}\,\Omega\text{m}$, which, although differing from the value reported in the literature, $\rho_{xx}(300) = 3 \times 10^{-6}\,\Omega\text{m}$ [44], is still closer to this reference than the bulk value of $\rho_{xx}(300) = 6.06 \times 10^{-7}\,\Omega\text{m}$. The resistivity of the thin film exhibits a linear dependence over a broad temperature range, extending from approximately 20 K to 300 K, whereas the bulk material shows linear behavior only over a narrower range. Moreover, the bulk material demonstrates a greater residual resistance ratio compared to the thin film.

The previously described trend persists when examining the ordinary magnetoresistance at the maximum field of ± 13 T as shown in Figure 5.2. The difference between bulk and thin film remains on the order of magnitude of 100 across all temperatures, with the OMR being significantly higher in the bulk material than in the thin film. This aligns with the observed differences in mobilities, where the carrier mobility in the bulk is notably

higher than in the film. It is also insightful to explore the temperature dependence of the OMR in both systems. In the bulk material, the OMR appears to exhibit an 1/T dependence on temperature at certain points. At higher temperatures, the OMR approaches zero, indicating that phonon scattering dominates, and the magnetic field has a minimal effect. In contrast, the OMR in the thin film demonstrates a more linear decrease with increasing temperature, although fewer temperature data points were measured for the thin film compared to the bulk. Notably, in the temperature range from 50 K to 100 K, the OMR drops significantly in the bulk material, whereas the thin film shows a nearly constant reduction over the same range. This disparity highlights distinct transport mechanisms and the stronger impact of temperature on the bulk material's magnetoresistance.

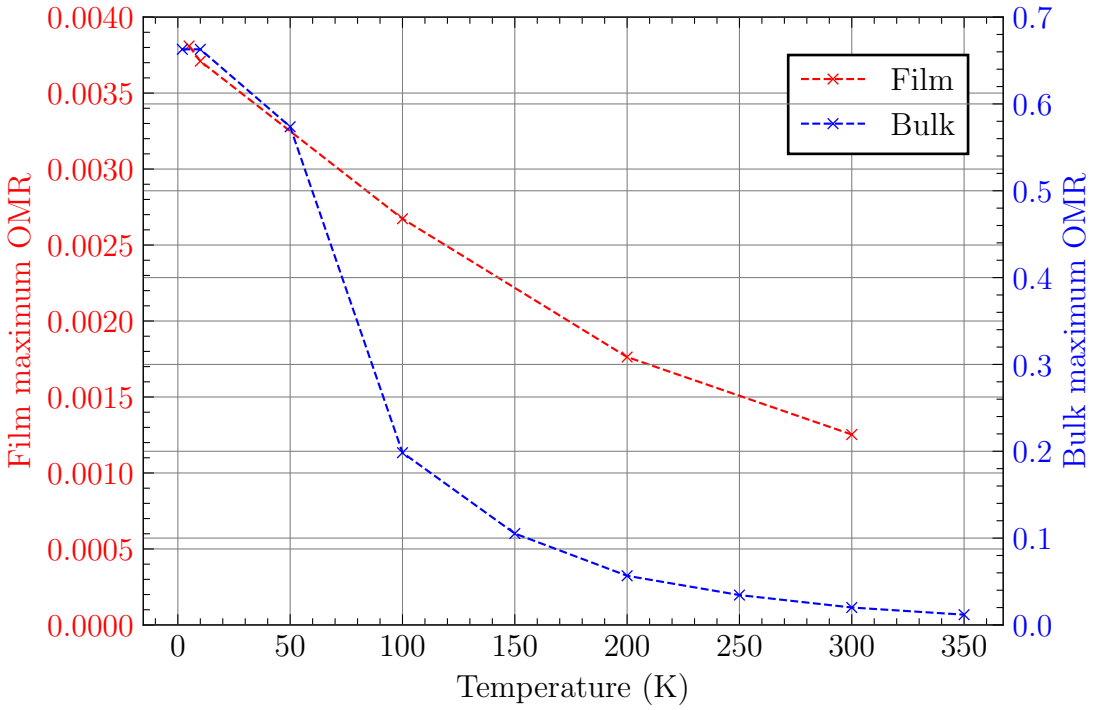

Figure 5.2: Comparison of OMR in bulk and thin film at maximum field ±13 T at various temperatures.

Figure 5.3 displays the Hall resistivity of the bulk sample along with its corresponding single-band model fit, as well as the Hall resistivity of the thin film at 10 K. The most striking difference between the bulk and thin film samples is the slope change observed in the bulk Hall resistivity, likely indicating the involvement of at least one additional carrier type in the transport process, as discussed in detail in Section 4.2. This characteristic slope change, occurring at $|\mu_0 H_z| \approx 1.3$ T, is absent in the thin film Hall resistivity. Despite this difference, the overall dominant slope remains negative in both systems, indicating predominantly hole-like transport. Interestingly, the carrier density derived from the single-band fit of the bulk data aligns well with the single-carrier fit of the thin film, showing a density mismatch of only ≈ 13 %. However, the mismatch in mobilities between the respective single-band fits is significantly larger, at ≈ 680 %. The reason for the differing mismatches lies in the distinct contributions of carrier density and mobility in the single-band transport model. In the Hall resistivity, described by

$$\rho_{yx} = \frac{B}{n_h e}, \tag{44}$$

only the carrier density n_h plays a role. In contrast, the longitudinal resistivity depends on both the carrier density and mobility, expressed as

$$\rho_{xx} = \frac{1}{n_h e \mu_h}. \tag{45}$$

As shown, the longitudinal resistivity differs significantly between the bulk and thin film, reflecting the pronounced discrepancy in mobilities. This observation, along with the absence of any evidence for a spin-flip or spin-flop transition in SQUID measurements, which aligns with ab initio calculations, supports the hypothesis of multiple carrier types in the bulk material. Additionally, no transition is observed in the thin film within the measured field range of $|\mu_0 H_z| = 13$ T. In conclusion, while introducing multiple carriers provides a better fit for the longitudinal and transverse resistivities in bulk, several indications suggest that the transport behavior in bulk CrSb is primarily governed by one electron band and one hole band, as confirmed by the MSA.

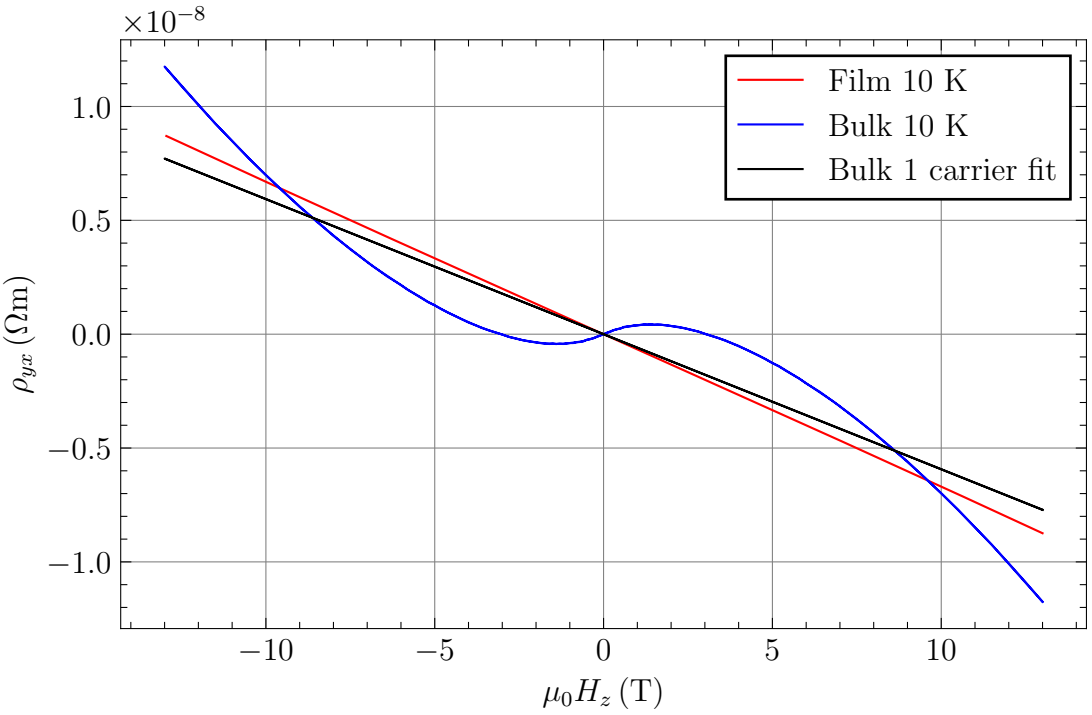

Figure 5.3: Comparison of Hall resistivity of bulk and thin film at 10 K as well as the single band fit of the bulk.

At this point, several reasons for the differing transport behavior between bulk crystals and thin films shall be discussed. The first factor is the distinct growth processes of the materials. While thin films are grown over the course of a few hours, the CVT process used for bulk crystals spans several days. This extended growth time allows the bulk material to more closely approach thermodynamic equilibrium, typically resulting in higher purity with fewer defects or vacancies. Although STEM images provide structural insights, it remains uncertain whether the film maintains perfect epitaxy across the entire sample. Additionally, point defects are challenging to detect in STEM imaging. Differences in purity and

composition inherently lead to variations in carrier scattering and, consequently, transport behavior. The presence of impurities can further lead to localization effects, as electron wavefunctions become hindered. These effects are more likely to occur in thin films due to the reduced freedom of carrier movement. This brings us to the next major contributing factor: dimensionality. In thin films, carrier movement is significantly restricted in the out-of-plane direction, whereas in bulk crystals, three-dimensional carrier transport cannot be excluded. In our analysis, the movement of carriers along the $\hat{z}$-direction was entirely neglected by employing the two-dimensional resistivity and conductivity tensor. Additionally, the placement of electrical contacts introduces variability: in bulk samples, contact alignment does not guarantee a well-defined current direction, while lithographically patterned Hall bars in thin films ensure precise current pathways. Geometrical factors also introduce potential surface and interface effects with adjacent layers, in our case PtSb, in thin films — effects that are naturally absent in bulk crystals.

5.1 Summary and Outlook

In summary, this work provides a comprehensive investigation of altermagnetic Chromium Antimonide (CrSb) in both bulk and epitaxial thin-film forms. Magnetometry confirms the vanishing net magnetization, while X-ray diffraction validates the hexagonal NiAs phase and structural quality. Magnetotransport studies reveal significant differences between the bulk and thin films, including a pronounced nonlinear Hall resistivity in bulk, attributed to multi-carrier transport with high-mobility carriers, which is absent in thin films. Carrier analysis indicates dominant hole-like transport in both systems but highlights vastly differing carrier densities and mobilities. High-field measurements did not reveal spin-flop, spin-flip transitions, or evidence of the anomalous Hall effect. These findings underscore the distinct transport dynamics and magnetic properties of CrSb in its bulk and thin-film forms.

Although none of the measurements presented in this work exhibit characteristics that can be exclusively attributed to altermagnetism, as distinct from antiferromagnetism, it remains important to recognize that CrSb is classified as an altermagnet according to theoretical symmetry considerations [8]. Additionally, experimental evidence of spin-splitting has been confirmed [23, 24, 25], as discussed earlier. As previously noted, CrSb not only exhibits a relatively high Néel temperature but also demonstrates substantial exchange and anisotropy fields compared to other altermagnets like MnTe [45]. These factors complicate the detection of spin-flop transitions and, consequently, the anomalous Hall effect. While the observed nonlinear slope in the Hall resistivity of the bulk material might initially suggest an interpretation as the AHE, it is instead attributed to multiband physics. This conclusion is supported by the absence of evidence for magnetic reorientations in SQUID magnetometry and aligns with the findings reported in Ref. [46].

As a closing remark, the study of altermagnetic CrSb presents many opportunities for further exploration. For example, preliminary thermal Hall measurements show a similar field-dependent S-shape behavior as observed in the bulk transport data, suggesting a potential link between these observations and the magnetotransport results presented in this work. Additionally, the quantum oscillations observed at high magnetic fields warrant further examination. It would also be valuable to dope the material in such a way that it reduces the magnetic anisotropy or induces a reorientation of the magnetic moments within the crystal, allowing the magnetic easy axis to align in a direction other than the c-axis. This could potentially enable the observation of the anomalous Hall effect.

Bibliography

[1] J. Shalf. The future of computing beyond Moore's law. *Philosophical Transactions of the Royal Society A: Mathematical, Physical and Engineering Sciences*, 378(2166):20190061, January 2020.

[2] N. Ul Mustafa, A. Armejach, O. Ozturk, A. Cristal, and O. Unsal. Implications of non-volatile memory as primary storage for database management systems. In *2016 International Conference on Embedded Computer Systems: Architectures, Modeling and Simulation (SAMOS)*. IEEE, July 2016.

[3] J. Åkerman. Toward a Universal Memory. *Science*, 308(5721):508–510, April 2005.

[4] S. Bandyopadhyay and M. Cahay. *Introduction to Spintronics*. CRC Press, March 2008.

[5] T. Jungwirth, X. Marti, P. Wadley, and J. Wunderlich. Antiferromagnetic spintronics. *Nature Nanotechnology*, 11(3):231–241, March 2016.

[6] L. Néel. Magnetism and Local Molecular Field. *Science*, 174(4013):985–992, December 1971.

[7] V. Baltz, A. Manchon, M. Tsoi, T. Moriyama, T. Ono, and Y. Tserkovnyak. Antiferromagnetic spintronics. *Reviews of Modern Physics*, 90(1):015005, February 2018.

[8] L. Šmejkal, J. Sinova, and T. Jungwirth. Beyond Conventional Ferromagnetism and Antiferromagnetism: A Phase with Nonrelativistic Spin and Crystal Rotation Symmetry. *Physical Review X*, 12(3):031042, September 2022.

[9] J. M. D. Coey. *Magnetism and Magnetic Materials*. Cambridge University Press, January 2001.

[10] S. Blundell. *Magnetism in Condensed Matter*. Oxford University PressOxford, October 2001.

[11] E. Stoner. Collective electron ferromagnetism. *Proceedings of the Royal Society of London. Series A. Mathematical and Physical Sciences*, 165(922):372–414, April 1938.

[12] S. Oki, S. Yamada, N. Hashimoto, M. Miyao, T. Kimura, and K. Hamaya. Effect of Addition of Al to Single-Crystalline CoFe Electrodes on Nonlocal Spin Signals in Lateral Spin-Valve Devices. *Applied Physics Express*, 5(6):063004, May 2012.

[13] R. Gross and A. Marx. *Festkörperphysik*. OLDENBOURG WISSENSCHAFTSVERLAG, August 2014.

[14] I. S. Jacobs. Spin-Flopping in MnF_2 by High Magnetic Fields. *Journal of Applied Physics*, 32(3):S61–S62, March 1961.

[15] C. Corrêa and K. Výborný. Electronic structure and magnetic anisotropies of antiferromagnetic transition-metal difluorides. *Physical Review B*, 97(23):235111, June 2018.

[16] L. Šmejkal, J. Sinova, and T. Jungwirth. Emerging Research Landscape of Altermagnetism. *Phys. Rev. X*, 12:040501, Dec 2022.

[17] D. B. Litvin. Spin point groups. *Acta Crystallographica Section A*, 33(2):279–287, March 1977.

[18] D.B. Litvin and W. Opechowski. Spin groups. *Physica*, 76(3):538–554, September 1974.

[19] L. Néel. Some New Results on Antiferromagnetism and Ferromagnetism. *Reviews of Modern Physics*, 25(1):58–63, January 1953.

[20] G. Dresselhaus. Spin-Orbit Coupling Effects in Zinc Blende Structures. *Physical Review*, 100(2):580–586, October 1955.

[21] H. C. Koo, S. B. Kim, H. Kim, T. Park, J. W. Choi, K. Kim, G. Go, J. H. Oh, D. Lee, E. Park, I. Hong, and K. Lee. Rashba Effect in Functional Spintronic Devices. *Advanced Materials*, 32(51), September 2020.

[22] J. Krempaský, L. Šmejkal, S. W. D'Souza, M. Hajlaoui, G. Springholz, K. Uhlířová, F. Alarab, P. C. Constantinou, V. Strocov, D. Usanov, W. R. Pudelko, R. González-Hernández, A. Birk Hellenes, Z. Jansa, H. Reichlová, Z. Šobáň, R. D. Gonzalez Betancourt, P. Wadley, J. Sinova, D. Kriegner, J. Minár, J. H. Dil, and T. Jungwirth. Altermagnetic lifting of Kramers spin degeneracy. *Nature*, 626(7999):517–522, February 2024.

[23] S. Reimers, L. Odenbreit, L. Šmejkal, V. Strocov, P. Constantinou, A. Hellenes, R. Jaeschke Ubiergo, W. Campos, V. Bharadwaj, A. Chakraborty, T. Denneulin, W. Shi, R. Dunin-Borkowski, S. Das, M. Kläui, J. Sinova, and M. Jourdan. Direct observation of altermagnetic band splitting in CrSb thin films. *Nature Communications*, 15(1), March 2024.

[24] M. Zeng, M. Zhu, Y. Zhu, X. Liu, Xi. Ma, Y. Hao, P. Liu, G. Qu, Y. Yang, Z. Jiang, K. Yamagami, M. Arita, X. Zhang, T. Shao, Y. Dai, K. Shimada, Z. Liu, M. Ye, Y. Huang, Q. Liu, and C. Liu. Observation of Spin Splitting in Room-Temperature Metallic Antiferromagnet CrSb. *Advanced Science*, 11(43), September 2024.

[25] G. Yang, Z. Li, S. Yang, J. Li, H. Zheng, W. Zhu, Z. Pan, Y. Xu, S. Cao, W. Zhao, A. Jana, J. Zhang, M. Ye, Y. Song, L. Hu, L. Yang, J. Fujii, I. Vobornik, M. Shi, H. Yuan, Y. Zhang, Y. Xu, and Y. Liu. Three-dimensional mapping and electronic origin of large altermagnetic splitting near Fermi level in CrSb, 2024.

[26] J. Yuan, Y. Song, X. Xing, and J. Chen. Magnetic structure and uniaxial negative thermal expansion in antiferromagnetic CrSb. *Dalton Transactions*, 49(48):17605–17611, 2020.

[27] S. Abe, T. Kaneko, M. Ohashi, H. Yoshida, and K. Kamigaki. Magnetic Properties of CrSb. *Journal of the Physical Society of Japan*, 53(8):2703–2709, August 1984.

[28] K. Momma and F. Izumi. VESTA 3 for three-dimensional visualization of crystal, volumetric and morphology data. *Journal of Applied Crystallography*, 44(6):1272–1276, October 2011.

[29] W. J. Takei, D. E. Cox, and G. Shirane. Magnetic Structures in the MnSb-CrSb System. *Physical Review*, 129(5):2008–2018, March 1963.

[30] M. Binnewies, R. Glaum, M. Schmidt, and P. Schmidt. Chemical Vapor Transport Reactions – A Historical Review. *Zeitschrift für anorganische und allgemeine Chemie*, 639(2):219–229, February 2013.

[31] J. H. Zhao, F. Matsukura, K. Takamura, E. Abe, D. Chiba, and H. Ohno. Room-temperature ferromagnetism in zincblende CrSb grown by molecular-beam epitaxy. *Applied Physics Letters*, 79(17):2776–2778, October 2001.

[32] J. Thornton. Magnetron sputtering: basic physics and application to cylindrical magnetrons. *Journal of Vacuum Science and Technology*, 15(2):171–177, March 1978.

[33] A. M. Miller, Me. Lemon, M. A. Choffel, S. R. Rich, F. Harvel, and D. C. Johnson. Extracting information from X-ray diffraction patterns containing Laue oscillations. *Zeitschrift für Naturforschung B*, 77(4–5):313–322, March 2022.

[34] N. Ashcroft. *Solid state physics*. Holt, Rinehart and Winston, 1976.

[35] E. H. Hall. On a New Action of the Magnet on Electric Currents. *American Journal of Mathematics*, 2(3):287, September 1879.

[36] T. Fujita, H. Okada, K. Koyama, K. Watanabe, S. Maekawa, and M. W. Chen. Unusually Small Electrical Resistance of Three-Dimensional Nanoporous Gold in External Magnetic Fields. *Physical Review Letters*, 101(16):166601, October 2008.

[37] G. Binasch, P. Grünberg, F. Saurenbach, and W. Zinn. Enhanced magnetoresistance in layered magnetic structures with antiferromagnetic interlayer exchange. *Physical Review B*, 39(7):4828–4830, March 1989.

[38] W. A. Beck and J. R. Anderson. Determination of electrical transport properties using a novel magnetic field-dependent Hall technique. *Journal of Applied Physics*, 62(2):541–554, July 1987.

[39] W. A. Beck. New techniques for mobility spectrum analysis. *Journal of Applied Physics*, 129(16), April 2021.

[40] A. I. Schindler and B. C. La Roy. Residual Resistance Ratio of Pure Iron. *Journal of Applied Physics*, 37(9):3610–3612, August 1966.

[41] M. Khoshenevisan, W. P. Pratt, P. A. Schroeder, and S. D. Steenwyk. Low-temperature resistivity and thermoelectric ratio of copper and gold. *Physical Review B*, 19(8):3873–3878, April 1979.

[42] B. Wiendlocha, S. Misra, A. Dauscher, B. Lenoir, and C. Candolfi. Residual resistivity as an independent indicator of resonant levels in semiconductors. *Materials Horizons*, 8(6):1735–1743, 2021.

[43] D. Cvijović. The Bloch-Gruneisen function of arbitrary order and its series representations. *Theoretical and Mathematical Physics*, 166(1):37–42, January 2011.

[44] T. Suzuoka. An Electrical Resistance Study of the System $(Cr_xMn_{1-x})Sb$. *Journal of the Physical Society of Japan*, 12(12):1344–1347, December 1957.

[45] R. D. Gonzalez Betancourt, J. Zubáč, R. Gonzalez-Hernandez, K. Geishendorf, Z. Šobáň, G. Springholz, K. Olejník, L. Šmejkal, J. Sinova, T. Jungwirth, S. T. B. Goennenwein, A. Thomas, H. Reichlová, J. Železný, and D. Kriegner. Spontaneous Anomalous Hall Effect Arising from an Unconventional Compensated Magnetic Phase in a Semiconductor. *Physical Review Letters*, 130(3):036702, January 2023.

[46] T. Urata, W. Hattori, and H. Ikuta. High mobility charge transport in a multicarrier altermagnet CrSb. *Physical Review Materials*, 8(8):084412, August 2024.

[47] S. Dutta, K. Sankaran, K. Moors, G. Pourtois, S. Van Elshocht, J. Bömmels, W. Vandervorst, Z. Tőkei, and C. Adelmann. Thickness dependence of the resistivity of platinum-group metal thin films. *Journal of Applied Physics*, 122(2), July 2017.

[48] M. Filoche and S. Mayboroda. Universal mechanism for Anderson and weak localization. *Proceedings of the National Academy of Sciences*, 109(37):14761–14766, August 2012.

Acknowledgements

At this point, I would like to mention some people who contributed to this work. First, I want to thank Dominik, Jörg, and Helena, who made this thesis possible by offering a topic, providing guidance, engaging in discussions, and allowing me to stay in Prague throughout the process. Further, I would like to thank Satya, not only for growing the measured films but also for the countless times explaining various concepts to me and sparking my interest. Another thank you goes to Jiří for providing me with high-quality bulk material. I would also like to thank Tonda, Zbyněk, and Honza for their guidance in the labs of Vektorak, the cleanroom, and PPMS. Additionally, I am grateful to Toni and Sajal for their support during the high-field experiments. Further I want to thank Karel, Philipp and Michał for the theoretical input of this work. Finally, I want to express my gratitude to Vít, Filip, and Kamil for the interesting coffee breaks and discussions.

Declaration of Authorship

Ich habe die Arbeit selbständig verfasst, keine anderen als die angegebenen Quellen und Hilfsmittel benutzt und bisher keiner anderen Prüfungsbehörde vorgelegt. Außerdem bestätige ich hiermit, dass die vorgelegten Druckexemplare und die vorgelegte elektronische Version der Arbeit identisch sind, dass ich über wissenschaftlich korrektes Arbeiten und Zitieren aufgeklärt wurde und dass ich von den in § 24 Abs. 6 vorgesehenen Rechtsfolgen Kenntnis habe.

Unterschrift

Ort, Datum